AGU PUBLICATIONS

JGR

Journal of Geophysical Research: Atmospheres

RESEARCH ARTICLE

10.1002/2013JD020709

Key Points:
- Uncertainties in ice microphysics outweigh uncertainties in initial conditions
- Ice fall speeds are the leading uncertainty affecting cirrus radiative impact
- Sensitivity of cirrus properties and radiative impact is largest at midlatitudes

Correspondence to:
A. Muhlbauer,
andreasm@atmos.washington.edu

Citation:
Muhlbauer, A., E. Berry, J. M. Comstock, and G. G. Mace (2014), Perturbed physics ensemble simulations of cirrus on the cloud system-resolving scale, *J. Geophys. Res. Atmos.*, *119*, doi:10.1002/2013JD020709.

Received 13 AUG 2013
Accepted 23 MAR 2014
Accepted article online 27 MAR 2014

Perturbed physics ensemble simulations of cirrus on the cloud system-resolving scale

Andreas Muhlbauer[1], Elizabeth Berry[2], Jennifer M. Comstock[3], and Gerald G. Mace[2]

[1]Joint Institute for the Study of the Atmosphere and Ocean, University of Washington, Seattle, Washington, USA, [2]Department of Atmospheric Sciences, University of Utah, Salt Lake City, Utah, USA, [3]Pacific Northwest National Laboratory, Richland, Washington, USA

Abstract In this study, the effect of uncertainties in the parameterization of ice microphysical processes and initial conditions on the variability of cirrus microphysical and radiative properties are investigated in a series of cloud system-resolving perturbed physics ensemble (PPE) and initial condition ensemble (ICE) simulations. Three cirrus cases representative of midlatitude, subtropical, and tropical anvil cirrus are examined. The variability in cirrus properties induced by perturbing uncertain parameters in ice microphysics parameterizations outweighs the variability induced by perturbing the initial conditions in midlatitude and subtropical cirrus. However, in tropical anvil cirrus the variability spanned by the PPE and ICE simulations is on the same order of magnitude. Uncertainties in the parameterization of ice microphysical processes affect the vertical distribution of cloud fraction, ice water content, and cloud thickness, whereas cirrus cloud cover is only marginally affected. The top three uncertainties controlling the microphysical variability and radiative impact of cirrus clouds are the mode of ice nucleation, the number concentrations of ice nuclei available for heterogeneous freezing, and the threshold size of the parameterized ice autoconversion process. Uncertainties in ice fall speeds are of minor importance. Changes in the ice deposition coefficient induce only transient effects on the microphysical properties and radiative impacts of cirrus except in cases of very low ice deposition coefficients of about 0.05. Changes in the sulfate aerosol number concentration available for homogeneous freezing have virtually no effect on the microphysical properties and radiative impact of midlatitude and subtropical cirrus but a minor effect on tropical anvil cirrus.

1. Introduction

Cirrus clouds contribute to about 30% to the total high cloud cover but exhibit pronounced latitudinal variability ranging from 10 to 20% at midlatitudes to more than 50% in the tropics [*Wylie and Menzel*, 1999; *Sassen et al.*, 2008]. Cirrus clouds have a profound impact on the radiative energy balance of the Earth's atmosphere by partly reflecting incoming solar radiation back to space and absorbing and reemitting outgoing longwave radiation (OLR) back to the surface [*Ackerman et al.*, 1988; *Stephens et al.*, 1990]. Unlike low clouds for which the shortwave cloud forcing dominates, the net cloud radiative forcing of cirrus can be positive or negative and strongly depends on the microphysical (e.g., particle size distribution, ice number concentration, ice water content, and crystal shape) and macrophysical (e.g., cloud fraction, cloud thickness, and ice water path) properties of cirrus.

According to recent studies, cirrus clouds are the dominant contributor to the longwave cloud feedback in global climate models (GCMs) [*Zelinka et al.*, 2012] but uncertainties regarding the magnitude of the cirrus cloud forcing and its role for climate sensitivity remain. These uncertainties are largely tied to an incomplete understanding of physical and dynamical processes controlling the microphysical evolution and the life time of cirrus as well as deficiencies in representing the observed vertical distribution and spatiotemporal variability of cirrus in GCMs [e.g., *Joos et al.*, 2008; *Gettelman et al.*, 2010].

Perturbed physics ensemble (PPE) experiments with GCMs suggest that one of the leading factors contributing to the spread in climate sensitivity among GCM simulations are ice fall speeds because they affect the ice particle loss through sedimentation and control the ice water path (IWP) and cirrus cloud coverage [*Sanderson et al.*, 2008]. Ice terminal fall velocities are crucially dependent on the size of ice crystals as well as the relationships between ice particle mass and area and are fundamentally linked to the microphysical evolution of cirrus. Temperature and ice water content (IWC) are key variables used to parameterize ice

fall speeds based on observations. Previous studies found ice fall speeds to increase with increasing temperature and increasing IWC [e. g., *Heymsfield et al.*, 2002; *Heymsfield*, 2003; *Deng and Mace*, 2008; *Mitchell et al.*, 2011]. According to Doppler radar observations, the majority of ice mass is contained in ice crystal modes sedimenting on average with velocities of about 30–50 cm s^{-1} depending on the size of the ice particles [*Deng and Mace*, 2008]. A comparison of ice fall speeds from Doppler radar observations with the fall speed-diameter relationships used in several leading GCM cloud parameterizations suggests that model fall speed relationships differ substantially from one another and disagree with observations to a large extent [*Deng and Mace*, 2008]. Furthermore, uncertainties in the particle size distribution (PSD) and, in particular, the contributions from small (i.e., maximum dimension smaller than 50 μm) ice crystals to the total ice number concentrations have a profound impact on the longwave cirrus cloud forcing by enhancing the IWP and high cloud cover [*Mitchell et al.*, 2008]. GCM simulations suggest that the increase in the longwave cloud forcing may be most pronounced in the tropics because anvil cirrus form at high altitudes in the tropical upper troposphere and because the contribution of cirrus clouds to the global high cloud occurrence is largest in the equatorial regions [*Sassen et al.*, 2008].

Past studies concerning the growth of ice crystals at cold temperatures indicate that small values of the ice deposition coefficient may explain the occurrence of high ice number concentrations in cirrus and the persistence of regions with high ice supersaturation found in the upper troposphere [*Gierens et al.*, 2003]. Over the years, laboratory measurements of the ice deposition coefficient have led to little consensus regarding what is deemed to be a representative value for ice crystal growth or sublimation under typical upper tropospheric conditions, partly because different experimental techniques have been used to infer this quantity. *Magee et al.* [2006] find deposition coefficients in the range of 0.005–0.008 for temperatures in the cirrus regime whereas modeling studies provide little support for deposition coefficients below 0.1 at least on a global scale because the microphysical properties and radiative forcing of cirrus could not be reconciled with observations given a low ice deposition coefficient scenario [*Kay and Wood*, 2008; *Lohmann et al.*, 2008].

A further key microphysical uncertainty is the mode of ice nucleation in cirrus clouds (i.e., through either homogeneous or heterogeneous ice formation pathways) and the sensitivity of cirrus microphysics to changes in the number concentration of aerosols serving as ice nuclei (IN). Homogeneous freezing of aqueous solution droplets is an important mechanism for ice formation in cirrus clouds at temperatures below about −38°C, the temperature threshold for homogeneous freezing of pure liquid water. A prerequisite for the formation of ice crystals through homogeneous freezing is the availability of aqueous solution droplets (mainly sulfates and organics) in the upper troposphere and high ice supersaturation ratios exceeding a temperature-dependent threshold of at least 140% [*Koop et al.*, 2000]. In contrast, heterogeneous freezing operates in mixed-phase and ice clouds and forms ice on preexisting IN at temperatures warmer than about −38°C and at relative humidities with respect to ice of approximately 100% [*Cziczo et al.*, 2013]. Generally, the role of heterogeneous ice nucleation for ice formation in cirrus clouds is not very well understood and highly debated because the properties of aerosols serving as IN are not very well characterized and hard to measure. The ability of aerosols to act as IN is primarily a function of temperature and ice supersaturation but varies considerably depending on the mode of heterogeneous ice nucleation and physicochemical properties of the aerosols [e.g., *Hoose and Mohler*, 2012].

While the relative role of homogeneous and heterogeneous freezing in cirrus clouds is debated and no conclusive answers have been found, it affects the cirrus microphysical evolution and has important consequences for the climatic impact of cirrus as well as for aerosol indirect effects in cirrus clouds [*Liu et al.*, 2012; *Gettelman et al.*, 2012; *Kulkarni et al.*, 2012]. Many past studies have assumed that homogeneous freezing of solution droplets is the dominant ice nucleation mechanism at lower temperatures. This hypothesis has been supported partly because the vast majority of atmospheric aerosol particles are aqueous solutions of sulfates or organics [*Murphy et al.*, 1998] and partly because observed high ice particle concentrations in cirrus could be reconciled with model simulations only if homogeneous freezing was invoked as the dominant ice nucleation mechanism [*Sassen and Dodd*, 1988; *Jensen et al.*, 1998; *Karcher and Strom*, 2003; *Haag et al.*, 2003]. However, over the last couple of years there is mounting support from in situ aircraft observations pointing toward heterogeneous ice nucleation as the dominant mechanism for initiating ice in cirrus and a potentially diminishing role of homogeneous freezing [*Jensen et al.*, 2010; *Cziczo et al.*, 2013].

The key objective of this study is to analyze the sensitivity of the microphysical and macrophysical properties of cirrus to perturbations in the model physics and to assess the potential effect on the radiative impact

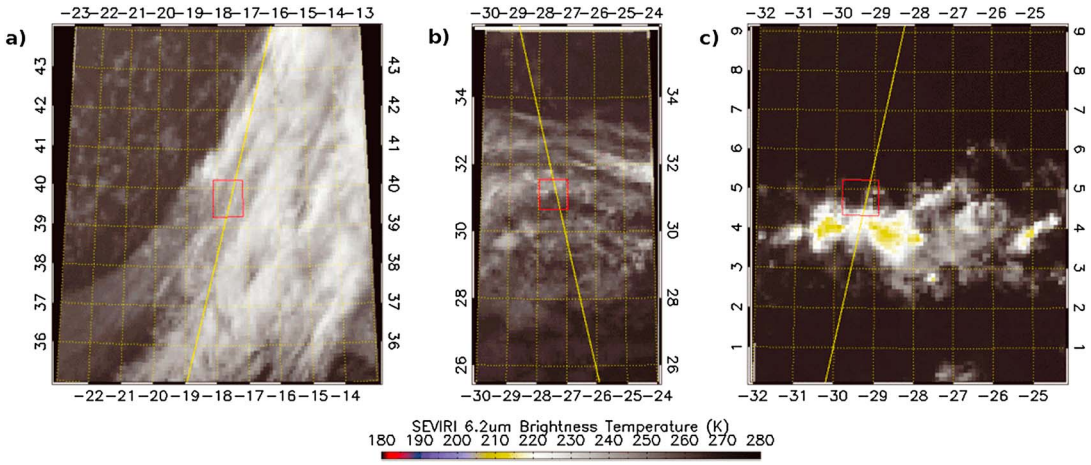

Figure 1. MSG SEVIRI 6.2 μm brightness temperature for the case studies representing (a) midlatitude, (b) subtropical, and (c) tropical cirrus. The yellow line indicates the A-Train track, and the red box indicates the study region. The time of observation is 12 March 2007 3:15 UTC for the midlatitude cirrus case, 16 February 2007 15:15 UTC for the subtropical cirrus case, and 27 April 2007 3:45 UTC for the tropical cirrus case.

of cirrus under various environmental conditions. A particular goal is to compare the sensitivity of cirrus properties caused by perturbations in the model physics (i.e., model error) to the sensitivity due to perturbations in the initial conditions (i.e., initial condition error) for various cirrus regimes. Since the microphysical and macrophysical properties of cirrus are inherently linked to the large-scale environmental conditions [e.g., *Berry and Mace*, 2013; *Muhlbauer et al.*, 2014], we expect to find the sensitivities to be different depending on the nature of the dynamical regime under which cirrus clouds form. The objectives and science questions are addressed by conducting a series of perturbed physics ensemble (PPE) and initial condition ensemble (ICE) simulations with a cloud system-resolving limited area model (CSRM).

The paper is structured as follows: section 2 introduces the cirrus case studies and observations. The model and experimental design are described in sections 3 and 4, respectively. Model simulations are evaluated with observations in section 5. Results of the PPE and ICE experiments are discussed in section 6, and conclusions are presented in section 7.

2. Case Studies and Observations

Three cases of cirrus over the Atlantic Ocean are examined in this study and represent midlatitude, subtropical, and tropical conditions, respectively. All case studies are identified and characterized by cirrus category based on a cluster analysis using cloud observations from active remote sensors aboard polar orbiting A-Train satellites as well as National Centers for Environmental Prediction/National Center for Atmospheric Research (NCAR) reanalysis fields over the Atlantic Basin [*Berry and Mace*, 2013]. In particular, we use observations from the cloud profiling radar (CPR) [*Im et al.*, 2006] and Cloud-Aerosol Lidar with Orthogonal Polarization (CALIOP) [*Winker et al.*, 2007] aboard the CloudSat and CALIPSO satellite, respectively. Each of the case studies is selected from a pool of observed cirrus cases closest to the cluster centroid and, thus, represents an archetypal example of the cirrus category.

Figure 1 shows infrared 6.2 μm wavelength brightness temperatures from the Spinning Enhanced Visible and Infrared Imager (SEVIRI) [*Schmetz et al.*, 2002] aboard the geostationary Meteosat Second Generation (MSG) satellite for the three cirrus cases. The meteorological fields from the European Centre for Medium-Range Weather Forecasts (ECMWF) ERA-Interim reanalysis are shown in Figure 2. Vertical cross sections of CloudSat radar reflectivity and retrieved total (liquid and ice) cloud water content of the sampled cloud fields are shown in Figure 3. Cirrus cloud occurrence and radar reflectivity are based on a cirrus cloud mask using a combination of CloudSat CPR and CALIOP lidar (2B-GEOPROF-LIDAR) [*Mace et al.*, 2009]. The combination of radar and lidar observations for cloud detection has significant benefits as it exploits the capabilities of both instruments in a synergistic way; that is, it combines the ability of the CPR to probe optically thick clouds with the higher sensitivity and vertical resolution of the lidar in detecting optically

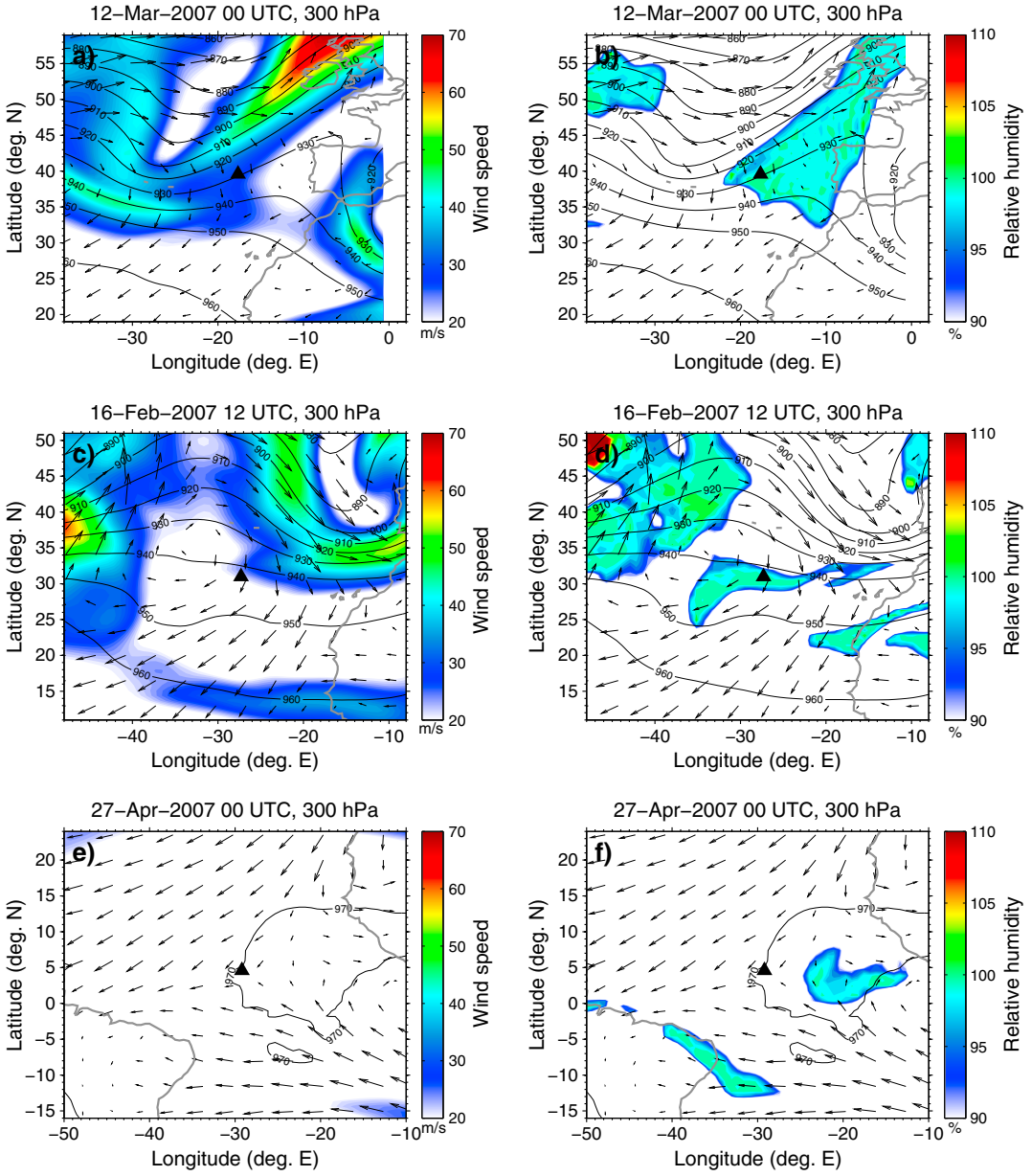

Figure 2. Upper level ECMWF analysis fields for the (a, b) midlatitude, (c, d) subtropical, and (e, f) tropical cirrus cases. Figures 2a, 2c, and 2e show wind speeds (shaded), wind direction (vectors), and geopotential heights (contoured) at the 300 hPa pressure level. Figures 2b, 2d, and 2f show relative humidity with respect to ice (shaded), geopotential heights (contoured), and wind direction (vectors) at the 300 hPa pressure level. Geographical boundaries are shown in gray, and the observed cirrus location is highlighted with a black triangle.

thin clouds and tenuous cloud tops that are below the CPR detection threshold of approximately −30 dBZ [*Tanelli et al.*, 2008]. Cirrus clouds detected by the lidar only are given a default value of −32 dBZ for radar reflectivity, which is below the minimum detectable signal of CloudSat. Regions of cirrus are identified based on column maximum radar reflectivity and temperature (from the ECMWF-AUX CloudSat data product) using the method described in *Mace et al.* [2006] and separated from other liquid and mixed-phase cloud types and cloud layers for the subsequent analysis of cirrus properties. Liquid and ice water content along the CloudSat track is retrieved using a suite of techniques described in *Zhang and Mace* [2006] and *Mace* [2010].

The first case study represents a midlatitude deep wave cirrus forming as a result of upper level divergence near the right entrance region of a jetstreak and was observed over the North Atlantic on 12 March 2007

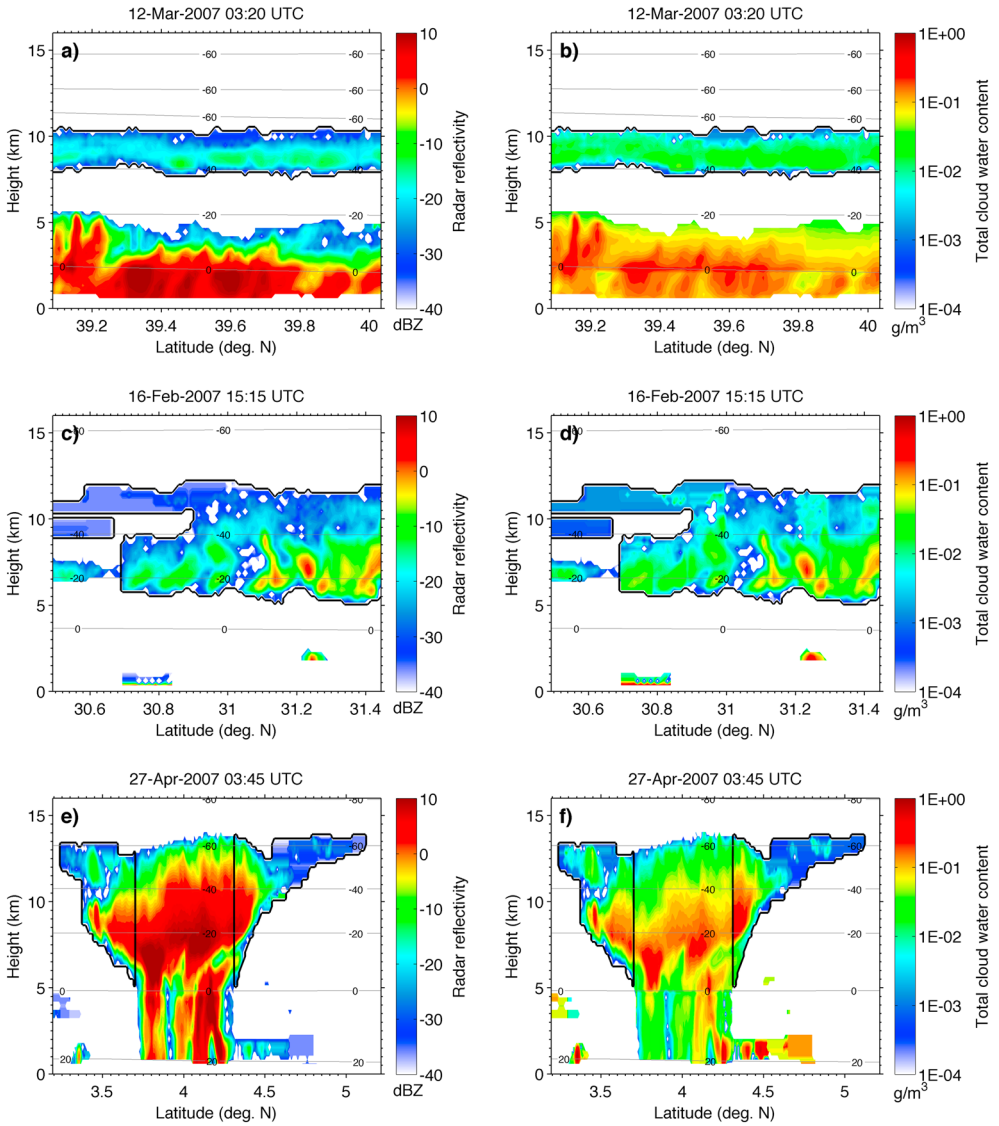

Figure 3. Vertical cross sections of (a, c, e) CloudSat CPR reflectivity and (b, d, f) total (liquid and ice) cloud water content for the midlatitude (Figures 3a and 3b), subtropical (Figures 3c and 3d), and tropical (Figures 3e and 3f) cirrus case. Cirrus cloud envelopes are derived following *Mace et al.* [2006] and are shown in black. Temperatures from the ECMWF analysis interpolated to the CloudSat CPR range bins are shown in gray.

(Figures 1 and 2). The deep wave cirrus regime is characterized by strong positive vorticity advection at upper levels and cold air advection and northwesterly flows in the lower troposphere typically associated with the passage of a cold front [*Berry and Mace*, 2013]. The cloud fields sampled by A-Train remote sensors consist of a deep layer of low- and midlevel mixed-phase clouds with cloud tops extending to about 6 km height and an approximately 2 km thick cirrus layer aloft with cloud base at around 8 km and cloud top at around 10 km height. Embedded in the cirrus layer are regions with higher radar reflectivities (up to about −10 dBZ) and higher IWC (up to approximately 0.1 g m^{-3}) indicative of larger ice particles sublimating near cloud base (Figure 3). Temperatures at cirrus cloud base are at and below about −40°C. Thus, it is possible to assume that homogeneous freezing of aqueous solution droplets may be the major microphysical mechanism for ice formation within the cirrus layer.

The second case study represents a cirrus cloud forming in an upper level subtropical ridge and was observed over the North Atlantic on 16 February 2007 (Figures 1 and 2). The ridge crest cirrus regime is characterized by weakly ascending vertical motions and weak negative vorticity advection near the axis of an upper level ridge. The sampled cloud fields show a single layer of thick cirrus between 5 and 12 km

Table 1. Setup of the CSRM Simulations

Domain	Grid Points	Grid Spacing	Levels	Time Step	Large-Scale Convection	Radiation Update Frequency
A	200 × 200	10 km	60	40 s	Parameterized	1 h^{-1}
B	300 × 300	4 km	100	20 s	Resolved	2 h^{-1}
C	400 × 400	2 km	125	10 s	Resolved	4 h^{-1}

altitude with sporadic patches of low boundary layer clouds underneath. The ridge crest cirrus layer exhibits slanted embedded fall streaks with high radar reflectivity and IWC (up to approximately 5 dBZ and several tenth g m^{-3}) indicative of sedimenting ice particles (i.e., virga) in a sheared environment close to cloud base (Figure 3). While the cirrus cloud tops are found well below −40°C, the cloud bases of the cirrus layer extend to temperatures much warmer than −20°C.

The third case study represents a dissipating tropical anvil cirrus triggered by a complex of mesoscale convective systems (MCSs) forming along a tropical convergence line with relatively weak influence from extratropical large-scale dynamics (Figures 1 and 2). The anvil cirrus was observed over the tropical North Atlantic region during 27 April 2007. The deep convective tower sampled by A-Train satellites extends from the boundary layer up to about 14 km altitude with anvil cirrus detraining from the convective core (Figure 3). Temperatures at the anvil tops are well below −60°C.

3. Model Description

The CSRM simulations are performed with the University of Washington version of the numerical weather prediction (NWP) model from the Consortium for Small-Scale Modeling (COSMO) (http://www.cosmo-model.org) [*Doms and Schättler*, 2002; *Baldauf et al.*, 2011]. COSMO is a limited area model that can be run for a variable range of grid spacings as a high-resolution NWP model or regional climate model [e.g., *Zubler et al.*, 2011].

COSMO employs a nonhydrostatic and fully compressible dynamical core. The discretized equations of motions are solved numerically with a two-time-level third-order Runge-Kutta scheme in combination with a fifth-order horizontal advection scheme. The time-splitting technique of *Wicker and Skamarock* [2002] is employed to solve the fast and slow modes separately in the model. All moisture variables and aerosols are transported using a fourth-order positive definite advection scheme [*Bott*, 1989].

The physical parameterizations in the model include the *Ritter and Geleyn* [1992] two-stream radiation scheme, a Mellor-Yamada turbulence scheme with a level 2.5 closure, and a prognostic equation for turbulent kinetic energy. Large-scale convection is parameterized following *Tiedtke* [1989]. The large-scale convection scheme is only employed at coarse resolution whereas for high-resolution simulations large-scale convection is assumed to be resolved by the finer model grid spacing. All physical tendencies are updated at every model time step except the tendencies due to large-scale convection and radiation. In order to decrease the computational burden of the simulations, large-scale convective tendencies are updated every tenth model time step and the update intervals for the radiative tendencies range between 15 min and 1 h depending on the horizontal model grid spacing (see Table 1 for details).

Bulk microphysical processes are treated with the double-moment mixed-phase bulk microphysics parameterization of *Morrison et al.* [2005, 2009] which is exclusively used throughout this study. Several modifications to the microphysics scheme are applied. First, the saturation water vapor pressure over ice and water is computed using the formulas of *Murphy and Koop* [2005], which give more accurate results for the saturation water vapor pressure over liquid water at cold temperatures. Second, the diffusional growth of ice is treated with the parameterization of *Harrington et al.* [2009] which explicitly accounts for the influence of the ice deposition coefficient and, therefore, surface kinetic effects on the growth of ice crystals. Third, the effects of aerosols on primary ice initiation by homogeneous and heterogeneous freezing are taken into account by replacing the existing ice nucleation parameterizations with the homogeneous freezing parameterization of *Koop et al.* [2000] and an empirical parameterization for heterogeneous freezing scheme, which is based on observations [*DeMott et al.*, 2010]. The number concentration of active IN is a function of temperature and the number concentration of accumulation mode aerosols larger than 0.5 μm. The observations used in the *DeMott et al.* [2010] parameterizations are based on Continuous Flow Diffusion

Chamber measurements and account for heterogeneous ice nucleation in the condensation, immersion, and deposition freezing modes. Because the formulation of microphysical tendency equations in the bulk microphysics scheme employs a time-splitting approach, the tendencies for ice number concentrations due to homogeneous and heterogeneous freezing are computed independently from one another and account for water vapor competition effects to within the length of the model time step, which is 10 s in case of the simulations with 2 km horizontal grid spacing. Fourth, the fallspeed-diameter relationships for ice crystals are parameterized as a function of temperature and IWC according to *Deng and Mace* [2008]. This ice fallspeed parameterization implicitly accounts for the observed variability of ice terminal fall velocities as a function of IWC and temperature and is based on multiple years of Doppler radar observations at the Atmospheric Radiation Measurement sites at the Southern Great Plains (SGP) and the Tropical Western Pacific (TWP) [*Deng and Mace*, 2008].

In order to facilitate a direct comparison of model output with CloudSat CPR observations, we implemented the Cloud Feedback Model Intercomparison Project Observation Simulator Package (COSP) [*Bodas-Salcedo et al.*, 2011]. COSP includes a cloud radar simulator for comparing model output with CloudSat CPR reflectivity profiles. All basic assumptions in the cloud microphysics scheme such as particle size distribution types and mass-dimensional relationships of hydrometeors are consistently treated in the instrument simulators.

4. Experimental Design and Model Setup

A sequence of nested CSRM simulations with horizontal grid spacings of 10 km, 4 km, and 2 km are conducted to capture the large-scale dynamics as well as the mesoscale dynamical features of the cirrus cloud systems. At the outermost grid with 10 km horizontal grid spacing, the CSRM is driven by initial and boundary conditions from the ECMWF analysis archive at 0.5° horizontal resolution and updated every 6 h. For the simulations on the inner domains (4 km and 2 km horizontal grid spacing), a grid nesting technique is used and the CSRM simulations are driven by initial and boundary conditions provided by the next coarser parent simulation and updated once per hour. The computational domains are chosen such that the study region is approximately centered in the model domain.

A stretched terrain-following coordinate system is used in the vertical with the model top placed at a height of 23.5 km. However, since a vertically stretched coordinate system would deteriorate the vertical model resolution at cirrus altitudes, we modified the stretched vertical coordinate system to accommodate additional model levels at cirrus altitudes between approximately 8 and 12 km as well as in the boundary layer. The minimum vertical grid spacing is 100 m in the cirrus layer and 20 m in the boundary layer. Details regarding the model setups, number of vertical levels, and computational domains are given in Table 1. The two outer domains (A and B in Table 1) are used to provide initial and boundary conditions for the innermost domain C and model simulations with 2 km horizontal grid spacing. Throughout this study we focus our analysis on the model simulations with 2 km horizontal grid spacing.

4.1. Baseline Simulations

For the baseline simulations, we use microphysical settings that are most plausible for each specific cirrus case study. Since observed ice fallspeeds are found to be higher in tropical environments than at midlatitudes [*Heymsfield*, 2003], we use the SGP observations to parameterize ice fallspeeds for the midlatitude and subtropical cirrus cases and the TWP observations for the tropical cirrus case (see Table 1 in *Deng and Mace* [2008] for details).

The ice autoconversion threshold size separating ice and snow categories in the bulk microphysics scheme is set to 100 μm which is somewhat in the middle of the range of possible values based on aircraft observations compiled by *Muhlbauer et al.* [2014]. The value for the vapor deposition coefficient is set to $\alpha_d = 0.1$ representing a relatively efficient ice crystal growth regime with little effect of surface kinetic effects. This choice is in line with previous studies suggesting that a value of $\alpha_d \geq 0.1$ produces the best match with observed cirrus optical depths distributions and top-of-the-atmosphere radiation budgets [*Kay and Wood*, 2008; *Lohmann et al.*, 2008].

The number concentrations of background sulfate aerosols and accumulation mode aerosols with diameters larger than about 0.5 μm are prescribed with N_{H2SO4}=270 cm^{-3} and $N_{>0.5}$=10 cm^{-3}, respectively, in the baseline simulations. In situ aircraft observations by *Minikin et al.* [2003] suggest that these aerosol number

Table 2. Microphysical Parameter Settings Used in the Control (CTL) Simulation

Parameter	Description	Value
f	Offset in the parameterization of ice fall speeds	0
α_d	Water vapor-ice deposition coefficient	0.1
D_i	Ice autoconversion threshold size	100 μm
N_{H2SO4}	Number concentrations of sulfate aerosols	270 cm^{-3}
$N_{>0.5}$	Number concentrations of accumulation mode aerosols	10 cm^{-3}

concentrations represent typical values found in the northern hemispheric upper troposphere. The number concentrations of aerosol particles larger than about 0.5 μm diameter are specified because observations often find a good correlation between the aerosol number concentrations at these sizes and the number concentrations of heterogeneous IN [*DeMott et al.*, 2010]. Since aerosols are not treated interactively in the model, aerosol and IN number concentrations are fixed in time and do not change properties as a function of past ice nucleation events. The baseline simulation serves as the control (CTL) and a summary of the parameter settings is provided in Table 2.

4.2. Perturbed Physics Ensembles

Perturbed physics ensemble (PPE) simulations have been conducted with GCMs to quantify the impact of uncertainties in the parameterized model physics on cloud forcing and climate sensitivity and to relate these model-induced uncertainties to uncertainties arising from internal variability caused by imperfect initial conditions [e.g., *Murphy et al.*, 2004; *Sanderson et al.*, 2008]. Here we conduct PPE simulations on a cloud system-resolving scale with a CSRM driven at much higher spatial resolutions than conventional GCMs. The perturbations in the model physics reflect current uncertainties in the parameterizations of ice microphysics such as ice fall speeds, ice autoconversion thresholds, ice deposition coefficients, the number concentrations of aerosols, and INs affecting ice nucleation as well as the mode of ice nucleation in cirrus. The perturbations in the initial conditions reflect the internal variability of cirrus properties in a given dynamical regime due to uncertainties in the initial conditions. The parameter settings in the PPE simulations are summarized in Table 3 and are discussed next.

4.2.1. Ice Fall Speeds

Terminal fall velocities of ice crystals at cirrus altitudes are typically much smaller than 2 m s^{-1} [e.g., *Heymsfield*, 2003] but critically depend on the size and shape of crystals. *Khvorostyanov and Curry* [2002] find a wide spread of the ice fallspeeds depending on the crystal habit and the diameter-fallspeed relationships used and occasionally exceeding a factor of 3 for ice crystals larger than about 100 μm diameter. However, ice fallspeed retrievals from ground-based Doppler radar greatly improve the uncertainty range of the mass median ice fall speeds and bound the uncertainty to within ±5 cm s^{-1} [*Deng and Mace*, 2008]. *Mitchell et al.* [2011] compared the ice fallspeed parameterization of *Deng and Mace* [2008] with their own parameterization of ice fall speeds derived from in situ observations from the Tropical Composition, Cloud and Climate Coupling (TC4) experiment and found overall close agreement between both parameterizations. However, they also find that the remaining differences between these parameterizations are a complicated function of temperature and IWC with a larger spread in ice fall speeds at low temperatures and for large values of

Table 3. Microphysical Parameter Range and Settings Used in the Perturbed Physics Ensemble (PPE) Simulations

Simulation	Experiment	Setting
LIFS	Low ice fallspeeds	$f = -5.0$ cm s^{-1}
HIFS	High ice fallspeeds	$f = +5.0$ cm s^{-1}
LIAC	Low ice autoconversion threshold	$D_i = 70$ μm
HIAC	High ice autoconversion threshold	$D_i = 120$ μm
LVDC	Low water vapor deposition coefficient	$\alpha_d = 0.005$
HVDC	High water vapor deposition coefficient	$\alpha_d = 1.0$
LSUC	Low sulfate aerosol concentration	$N_{H2SO4} = 45$ cm^{-3}
HSUC	High sulfate aerosol concentration	$N_{H2SO4} = 400$ cm^{-3}
LINC	Low accumulation mode aerosol concentration	$N_{>0.5} = 2$ cm^{-3}
HINC	High accumulation mode aerosol concentration	$N_{>0.5} = 30$ cm^{-3}
HOMO	Homogeneous freezing only	N/A
HETO	Heterogeneous freezing only	N/A

IWC. Throughout this study, we apply a simple offset or bias to alter the terminal fall velocities of the ice and snow categories in the PPE simulations in accordance with the uncertainty range derived from the Doppler radar observations (see Table 3).

4.2.2. Autoconversion of Ice

A critical and largely unconstrained parameter in bulk microphysics parameterizations is the maximum dimension threshold that artificially separates ice and snow categories. The size threshold used to separate ice and snow categories is also used in bulk microphysics schemes to parameterize the transfer of mass from the smaller ice to the larger snow category. This hydrometeor categorization introduces an artificial microphysical process in bulk microphysics schemes that is usually referred to as the autoconversion of ice. Most cloud microphysics parameterizations use a size threshold somewhere between 100 and 200 μm to separate ice and snow categories [*Reisner et al.*, 1998; *Morrison et al.*, 2005; *Morrison and Gettelman*, 2008]. The lower and upper bounds for the ice autoconversion threshold diameter used in the PPE simulations are based on averaged PSD measurements from a two-dimensional stereo probe flown aboard aircraft during the U.S. Department of Energy Small Particles in Cirrus field campaign [*Muhlbauer et al.*, 2014] and are given in Table 3.

4.2.3. Diffusional Growth of Ice

Another largely unconstrained quantity in ice microphysics parameterizations is the ice deposition coefficient, which is a material quantity describing the resistance of the ice lattice to take up water molecules from the surrounding supersaturated water vapor phase. Past studies have suggested that small values of the ice deposition coefficient may explain high number concentrations of ice crystals in cirrus clouds and the persistence of regions with high ice supersaturation found in the upper troposphere [e.g., *Gierens et al.*, 2003]. Over the years, laboratory measurements of the ice deposition coefficient have led to little consensus regarding what is deemed to be a representative value for ice crystal growth or sublimation under typical upper tropospheric conditions, partly because different technical approaches have been used in the experiments. *Magee et al.* [2006] found deposition coefficients in the range of 0.005–0.008 for temperatures in the cirrus cloud regime. Similar values are also used by *Harrington et al.* [2009] to investigate the impact of kinetically limited growth of ice crystals on the properties of cirrus clouds. Here we use a parameter range of 0.005–1 for the lower and upper bounds of the deposition coefficient in the PPE simulations (Table 3).

4.2.4. Ice Initiation, Aerosol, and Ice Nuclei Concentrations

Homogeneous freezing is an important mechanism for ice formation in cirrus clouds at temperatures below about −38°C whereas heterogeneous freezing is the primary mechanism for ice formation in mixed-phase and ice clouds at temperatures warmer than about −38°C (the homogeneous freezing threshold of pure liquid water droplets). The fact that aerosol particles can act as ice nuclei in different ice nucleation modes depending on the ambient temperature and supersaturation makes measuring ice nuclei concentrations difficult and inferences about heterogeneous ice nucleation uncertain.

A prerequisite for the formation of ice crystals through the homogeneous freezing pathway is the availability of aqueous solution droplets that form on sulfate aerosol particles in the upper troposphere (either sulfuric acid droplets or solution droplets formed by the deliquescence of ammonium sulfate below water saturation). The variability of aerosol particles in the upper troposphere is relatively large, and confident estimates of aerosol number concentrations are lacking mainly due to the dearth of representative measurements. Measurements of total aerosol number concentrations representative of background tropospheric aerosol during the Interhemispheric Differences in Cirrus Properties from Anthropogenic Emissions (INCA) campaign range from approximately 40 cm^{-3} in relatively remote environments of the Southern Hemisphere to more than 350 cm^{-3} in more continental environments such as the tropopause region over northern Europe [*Minikin et al.*, 2003]. The range of accumulation mode aerosol number concentrations (0.1–1 μm size range seen by the passive cavity aerosol spectrometer probe) found during the Interhemispheric Differences in Cirrus Properties from Anthropogenic Emissions (INCA) aircraft field campaign is approximately 2–11 cm^{-3} for the Southern Hemisphere and about 5–30 cm^{-3} for the Northern Hemisphere [*Minikin et al.*, 2003]. During INCA, most aerosol measurements were taken over remote continental regions at midlatitudes but some measurements of aerosol number concentrations in the subtropical and tropical upper troposphere are available from transfer flights to and from the Southern Hemisphere. Since the variability in aerosol number concentrations in the upper troposphere is not very well constrained, we take the lower bound of the Southern Hemispheric range and the upper bound of the Northern Hemispheric range as a rough guide

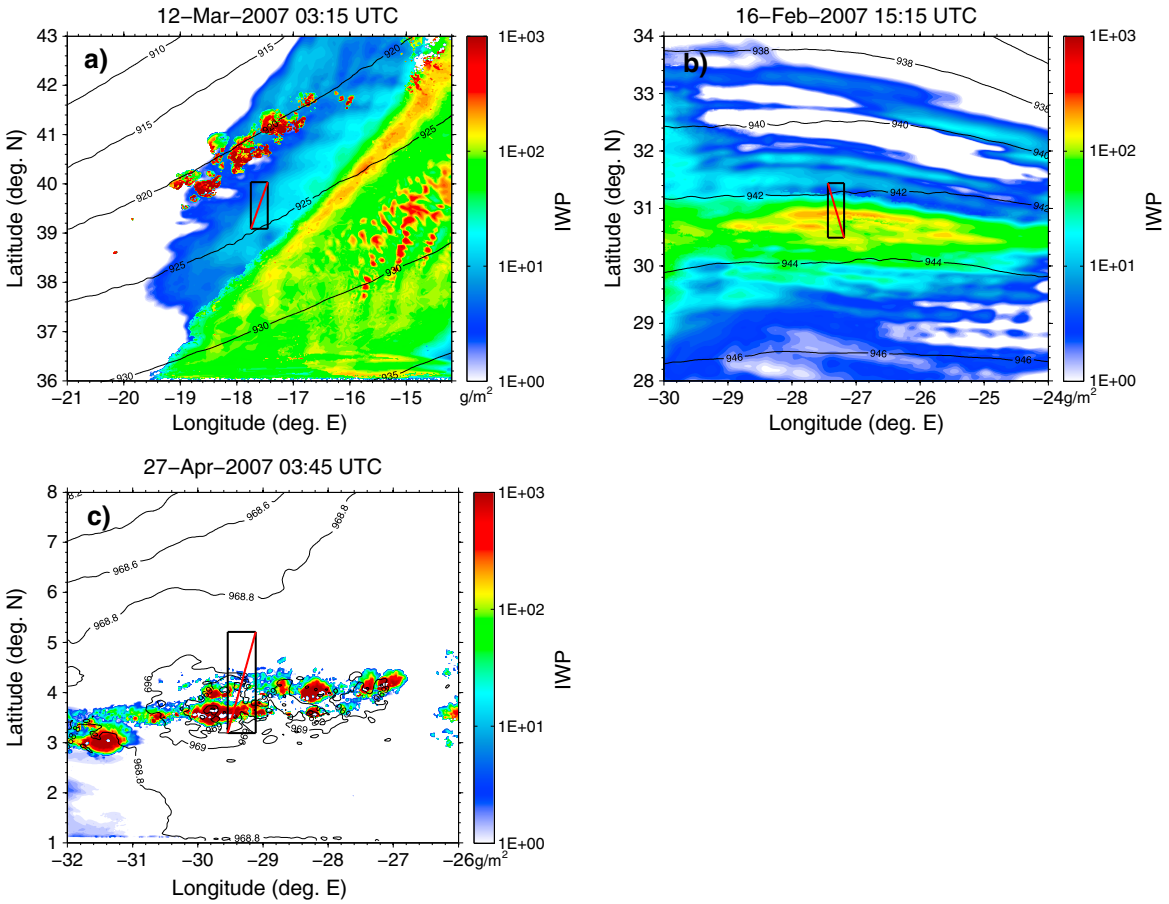

Figure 4. Ice water path (shaded) and geopotential heights at the 300 hPa pressure level (contours) in the control simulation for (a) the midlatitude, (b) subtropical, and (c) tropical cirrus cases. The portion of the CloudSat track shown in Figure 3 is indicated as a solid red line. The comparison region is indicated as a rectangular box with boundaries shown as solid black lines.

for the accumulation mode aerosol variability in the upper troposphere and bracket sulfate aerosol concentrations to within the range of 45 cm^{-3} to 400 cm^{-3} (see Table 3 for details).

Since the roles of homogeneous and heterogeneous ice nucleation for ice formation in cirrus clouds is not very well understood and highly debated, we perform additional PPEs by switching off the homogeneous/heterogeneous ice nucleation scheme thereby allowing for homogeneous freezing only (HOMO) and heterogeneous freezing only (HETO) scenarios.

4.3. Initial Condition Ensembles

In addition to the PPE simulations, a set of ensemble simulations is produced for each cirrus case study by slightly perturbing the initial and boundary conditions for temperature. The perturbations satisfy a normal distribution with zero mean and prescribed standard deviation σ. The perturbations for temperature T' are specified such that $T' = T + \sigma_T \mathcal{N}$ with $\sigma_T = 0.2$ K and $\mathcal{N}$ the standard normal distribution. The value for the standard deviation is derived from previous error analyses and reflect typical uncertainties in temperature measurements from radiosondes [*Miloshevich et al.*, 2003; *Turner et al.*, 2003]. The ICE simulations are realized by adding the random temperature to the initial temperature field and by perturbing the model inflow boundaries at every grid point between 8 km and 12 km height. Overall, 10 ICE simulations are performed for each cirrus case study by changing the seed value of the random number generator.

5. Model Evaluation

A systematic comparison of the model output with observations from MSG SEVIRI and CloudSat is performed for all case studies. The primary metrics for comparing model output with observations are vertical profiles of cloud fraction, simulated cloud radar reflectivity, and IWC. IWC is retrieved from the A-Train

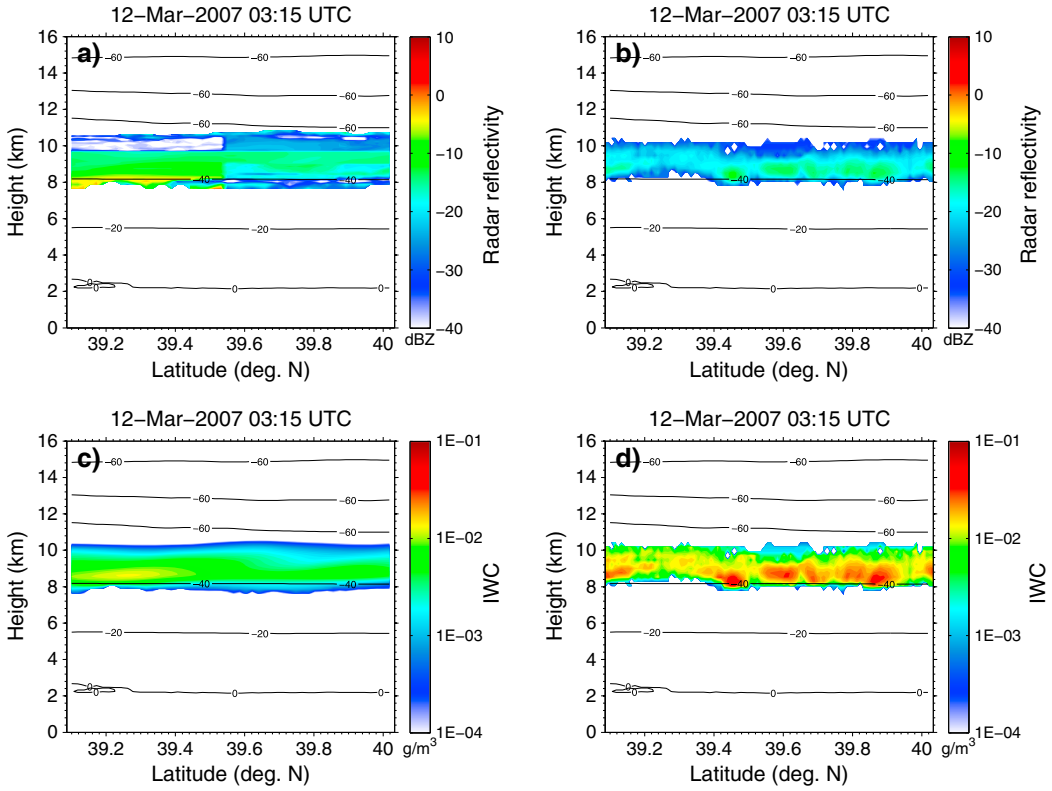

Figure 5. Vertical cross sections of (a, b) radar reflectivity and (c, d) ice water content for the midlatitude cirrus case. The control simulation is shown in Figures 5a and 5c, and the CloudSat observations are shown in Figures 5b and 5d. The model fields are averaged meridionally over the box shown in Figure 4. Ice water content in the model includes ice and snow categories. Only parts of the cloud field identified as cirrus are shown. Temperatures are shown as solid black contours.

observations using the retrieval algorithm of *Mace* [2010]. Since we are interested in uncertainties in the parameterization of ice microphysical processes, we focus our analysis and model evaluation on cirrus clouds only. This is achieved by consistently applying the cirrus identification algorithm of *Mace et al.* [2006] to the CloudSat observations and model output prior to comparison. In order to facilitate a direct comparison of model output with satellite observations, we implemented a suite of satellite instrument simulators as discussed in section 3.

Figure 4 shows the simulated ice water path (IWP) for all case studies at the time of the CloudSat overpass. In the midlatitude cirrus case, the cirrus forms ahead of an upper level trough whereas in the subtropical cirrus case the cloud field forms within an upper level ridge. Both the simulated midlatitude and subtropical cirrus cloud fields exhibit inhomogeneous banded structures and embedded pockets with higher cirrus density as shown in the satellite observations (Figure 1). The geographical location of the simulated cirrus cloud fields agrees reasonably well with the satellite observations, and the major cirrus features are nicely represented. In the tropical cirrus case, the simulated cloud fields show a line of tropical convection and anvil cirrus as in the satellite observations but the number of convective cores and the geographical alignment is not fully captured in the model simulations but, in fact, appears somewhat shifted toward the south. Although the reason for the slight misalignment regarding the location of the tropical MCS remains unclear, it may be caused by errors in the ECMWF analysis fields used to drive the regional model simulations. Larger errors in analysis fields may be expected given the remote location over tropical oceans where observations are generally infrequent and sparse.

Vertical cross sections of observed and simulated CloudSat radar reflectivity and IWC are shown in Figures 5, 6, and 7 for the midlatitude, subtropical, and tropical cirrus cases, respectively. For all cases, the major features of the cirrus such as the vertical cloud distribution, radar reflectivity, and IWC are reasonably well simulated given the uncertainties in the ECMWF initial and boundary conditions, the uncertainties

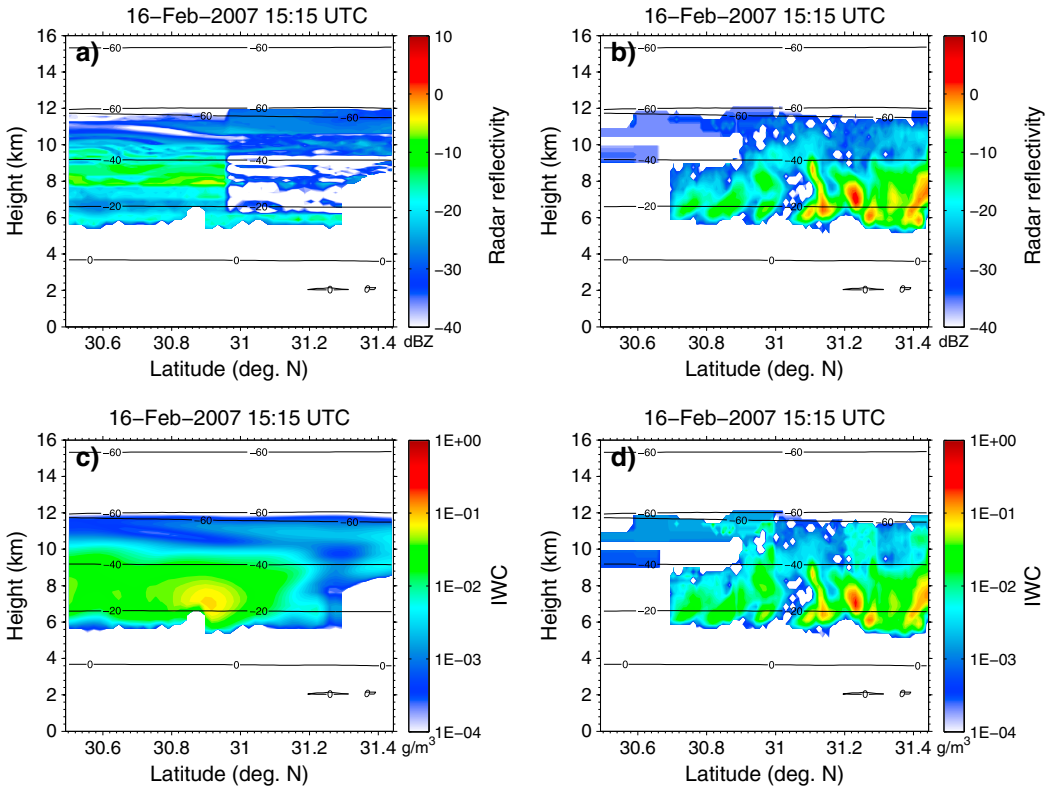

Figure 6. Same as Figure 5 but for the subtropical cirrus case.

associated with the forward calculation of radar reflectivities within COSP, and uncertainties pertaining to retrievals of IWC from radar observations. However, there are some deficiencies in the model simulations regarding some of the small-scale features. Since the vertical cross sections of the simulated cloud fields are averaged meridionally over an area considerably larger than the 2 km wide footprint of the CPR, we do not expect that the model represents these small-scale features that may not be representative of the cirrus cloud field on larger scales.

The vertical distributions of cloud fraction, radar reflectivity, and IWC are shown in Figure 8 for all cirrus cases. Overall, there is good qualitative agreement between the observations and the control simulation regarding the major features such as the vertical extent of the cirrus, and the vertical distribution of cloud fraction, radar reflectivity, and IWC. Most observations fall roughly within the range spanned by the ICE or PPE simulations. In the midlatitude cirrus case, the observed vertical profile of cloud fraction and the thickness of the cirrus layers is well captured by the model simulations and agrees with observations to within approximately 100 m, which corresponds to the vertical resolution of the model. The simulated vertical profile of CloudSat radar reflectivity agrees reasonably well with observations showing a general increase of radar reflectivity from cirrus cloud top toward the middle of the cloud followed by a decline in radar reflectivity toward cloud base. Throughout most parts of the cloud, the observed radar reflectivity falls within the uncertainty range spanned by the PPE simulations. The profile of IWC exhibits good qualitative agreement with the observations regarding the vertical distribution of IWC within the cloud and the location of maximum IWC at around 8.5 km height. However, cirrus IWC is grossly underestimated throughout the whole cirrus layer and the peak IWC is underestimated even for the largest values in the PPE simulations, which leads to about a factor of three discrepancy between the simulated and observed IWP. It is stressed, however, that the uncertainty in IWC retrievals is on the order of 70% as discussed in *Mace* [2010] and much larger than the uncertainty in the radar reflectivity. Overall, the variability in cirrus cloud properties induced by uncertainties in the ice microphysics clearly outweighs the variability due to uncertainties in the initial conditions in this case.

In the subtropical cirrus case, there is good qualitative agreement between the observed and simulated cirrus properties. Again, the variability in the PPE simulations is considerably larger than the variability in

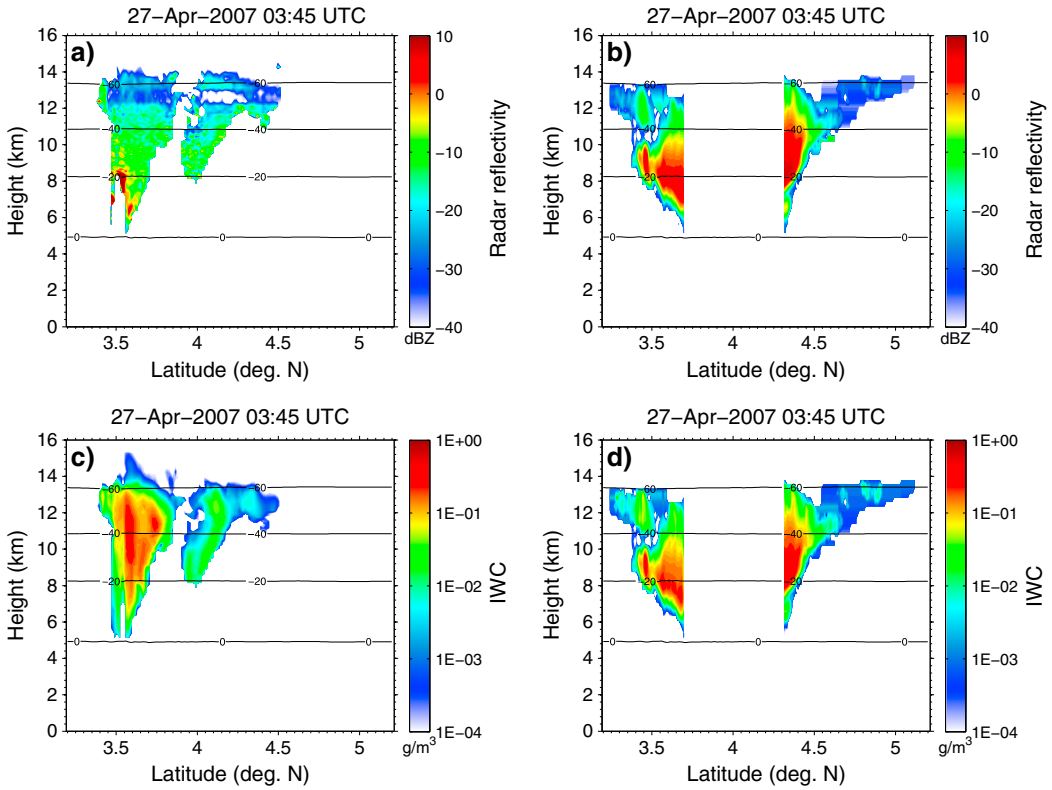

Figure 7. Same as Figure 5 but for the tropical cirrus case.

the ICE simulations suggesting that uncertainties in cirrus properties are driven primarily by microphysical uncertainties rather than uncertainties in the initial conditions. The observed cloud fraction is reasonably well represented in the simulations with slight overestimation between 8 km and 12 km. The cloud fraction is overestimated because the observed cirrus cloud layer exhibits patchiness with some clearing of individual cloud layers toward the southern edge of the cloud field as shown in Figures 3c and 3d. However, this rather small-scale cloud clearing is not represented in the simulations and may be a feature representative only for the narrow line of cirrus sampled by CloudSat. The location of cloud top exhibits virtually no variability in either the PPE or ICE simulations in this case but considerable variability is seen in the PPE simulations with respect to cloud base. Again, the vertical profiles of radar reflectivity and IWC exhibit reasonable qualitative agreement with the observations with some discrepancies in radar reflectivity between about 6 and 8 km. This is because the CloudSat observations show a number of small pockets with high radar reflectivity toward cloud base, which are not captured by the model simulations. Overall, the variability in the PPE simulations is considerably larger than the variability in the ICE simulations suggesting that the uncertainty induced by perturbing the parameterized ice microphysics is larger then the uncertainty induced by perturbing the initial conditions. In the subtropical cirrus case, cloud top height is quite insensitive to variations in the PPE simulations whereas cloud base is highly variable, which in turn affects cirrus cloud thickness and IWP and is discussed in greater detail in the next section.

In the tropical anvil cirrus case, the simulated cloud fraction is considerably smaller than the observations between about 5 and 15km whereas the vertical extent of the convective cloud is overestimated. The underestimation of cloud fraction in the simulation is caused by a smaller horizontal extent of the anvil cirrus, which is partly due to a misalignment of the location of the deep convective core between the observations and the simulation. The overestimation of the vertical cloud extent, however, is due to optically thin cirrus with only little IWC and radar reflectivities, which are well below the detection threshold of the CPR. In fact, the observed radar reflectivity falls within the range spanned by the PPE and ICE simulations and also compares nicely with the control simulation. In contrast to the midlatitude and subtropical cirrus cases, the sensitivity of the cirrus cloud fraction to perturbations in the initial conditions is about on the same order of magnitude than the sensitivity induced by perturbations in the parameterized ice microphysics.

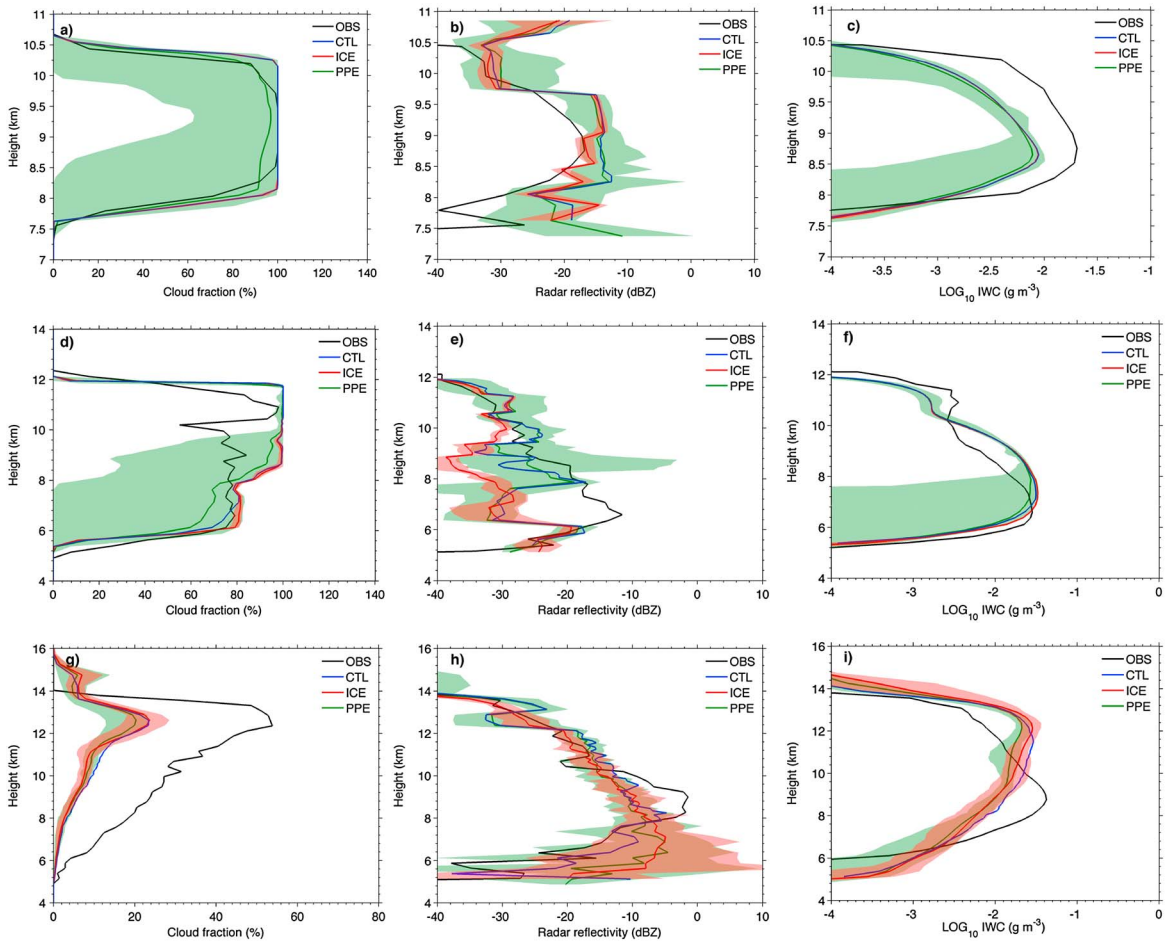

Figure 8. Vertical profiles of (a, d, g) cloud fraction, (b, e, h) radar reflectivity, and (c, f, i) ice water content for the midlatitude (Figures 8a, 8b, and 8c), subtropical (Figures 8d, 8e, and 8f), and tropical (Figures 8g, 8h, and 8i) cirrus cases. The vertical profiles are horizontally averaged over the CloudSat overpass region. Observations (OBS) are shown in black, and the control (CTL) simulation is shown in blue. Ensemble means are shown for the ICE (red) and PPE (green) simulations. The shaded areas represent the breadth of the ensemble distribution.

This emphasized the dynamical sensitivity of tropical convection and its potential impact on the microphysics of anvil cirrus.

Overall, there is reasonable agreement between the observations and the model simulations in all cirrus cases. The discrepancies between simulations and observations are generally higher for IWC than for radar reflectivity and tend to be largest in the midlatitude cirrus case. However, it is also stressed that observed IWC estimates used throughout this study are based on retrieval algorithms bearing considerable uncertainties. The variability in cirrus cloud profiles induced by uncertainties in microphysics outweighs the variability due to uncertainties in the initial conditions in both the midlatitude and subtropical cirrus cases. However, in the tropical anvil cirrus case, the variability due to uncertainties in microphysics and initial conditions is on the same order of magnitude.

6. Perturbed Physics Ensemble Simulations

The sensitivities of the cirrus microphysical and radiative properties for each case study are discussed in the subsequent section.

6.1. Midlatitude Cirrus Case

As expected, the changes in the cirrus microphysics affect the vertical cloud profile and the radiative impact of cirrus. The sensitivity of the vertical cirrus cloud fraction and IWC profiles in the PPE simulations is shown in Figures 9 and 10, respectively. As shown in Figure 9a, lower ice fall speeds (LIFS) increase the height of cloud base but decrease the cloud thickness due to a decrease in the sedimentation path length. At the

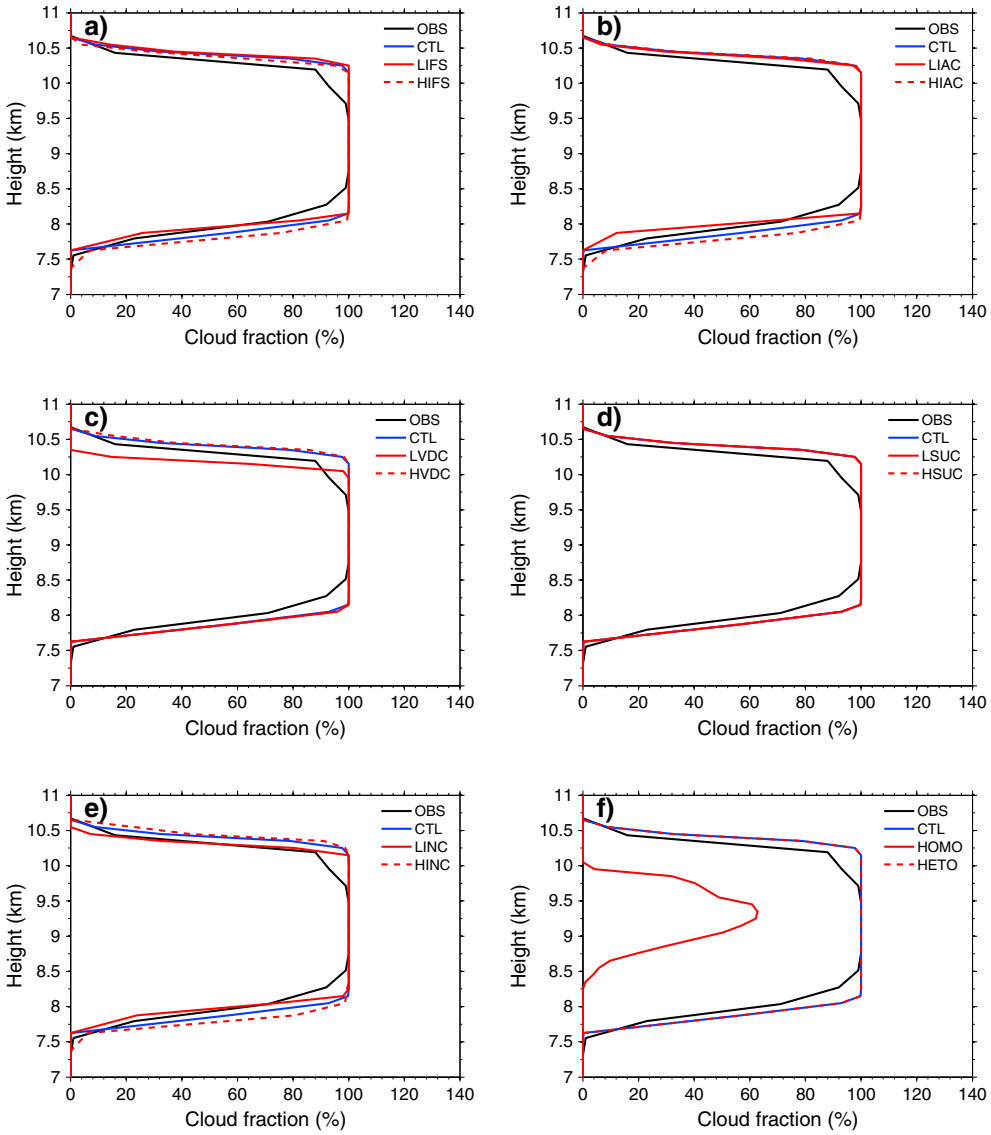

Figure 9. Vertical profiles of cloud fraction in the observations (black), the control simulation (blue), and the perturbed physics ensemble (PPE) simulations (red solid and dashed) for the midlatitude cirrus case. Figure panels refer to PPEs with changes in (a) ice fallspeeds, (b) ice autoconversion, (c) ice accommodation coefficient, (d) sulfate aerosol number concentrations, (e) heterogeneous ice nuclei concentrations, and (f) the mode of ice nucleation in cirrus.

same time, a decrease in the ice fall speeds leads to an increase in IWC due to increased ice crystal growth through vapor deposition in the supersaturated part of the cloud. This additional ice particle growth is possibly due to the increased residence time of ice particles in the ice supersaturated cirrus layers. Since IWP is a function of IWC and cloud thickness, the net effect on IWP is not immediately obvious. However, in this case, the gain in IWC outweighs the loss in cloud thickness leading to an overall increase in IWP in the simulation with decreased ice fall speeds (LIFS). The opposite is true in the simulation with increased ice fall speeds (HIFS).

A similar response in the physical cirrus properties is seen by changing the threshold size for ice autoconversion (simulation LIAC and HIAC; see Figure 9b). A decrease (increase) in the ice autoconversion threshold size leads to an increased (decreased) shift of ice mass from the slowly sedimenting ice particle category to the faster sedimenting snow category and therefore decreasing (increasing) IWP by reducing (enhancing) the time available for particle growth and enhancing (reducing) ice sedimentation. In terms of cloud fraction, the impact of changes in ice falls speeds and the size of the ice autoconversion threshold are largest at cloud base.

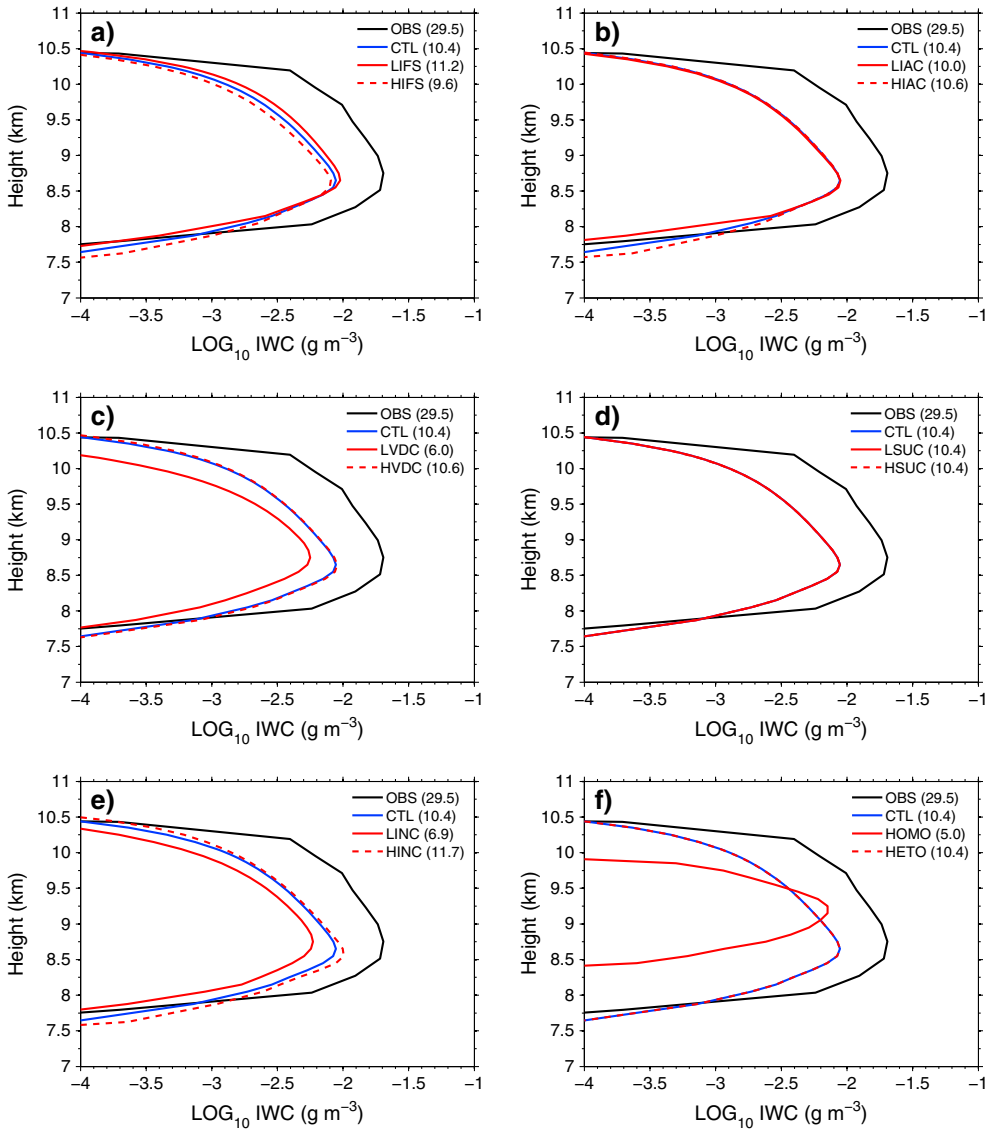

Figure 10. Same as Figure 9 but for ice water content (IWC). The IWP of each cirrus cloud profile is given in brackets in units of g m^{-2}.

In contrast, changing the value of the ice deposition coefficient (simulations LVDC and HVDC; see Figure 9c) affects the entire cirrus cloud profile in terms of IWC but the impact on cloud fraction is largest at cloud top. However, the implications of changing ice deposition coefficients are less straightforward to understand and some effects are not robust but rather transient in time. For example, within our study region, a lower (higher) value for the ice deposition coefficient leads to less (more) depositional growth and a lower (higher) cloud thickness and, thus, to a lower (higher) IWP. However, considering the effect on larger scales such as the whole cirrus cloud system rather than individual patches of cirrus as well as longer time scales, lower values of the ice deposition coefficient lead to higher ice supersaturations and, as time proceeds, to higher vapor deposition rates and a larger cirrus IWP. Also, we find little difference between the control simulation with vapor deposition coefficient of 0.1 and the simulation with vapor deposition coefficient equal to unity. This result is consistent with simulations performed by *Harrington et al.* [2009] who also found little difference in the evolution of cirrus IWP for ice deposition values in the range of approximately 0.1 to 1. Only very low values on the order of 0.005 as in our simulation LVDC have a significant and persistent effect on the cirrus IWP.

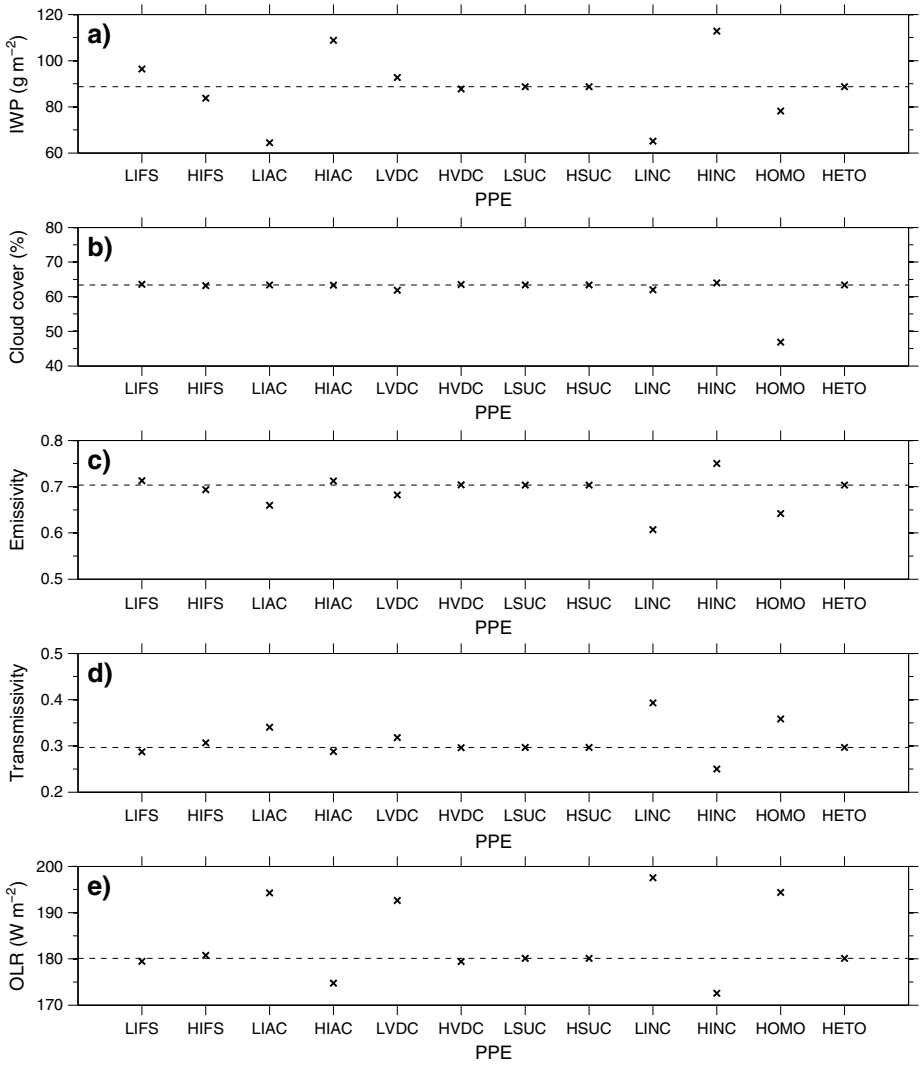

Figure 11. Domain-averaged values of (a) cirrus ice water path, (b) cloud cover, (c) longwave emissivity, (d) transmissivity, and (e) outgoing longwave radiation in the perturbed physics ensemble (PPE) simulations for the midlatitude cirrus cases. The domain-averaged values for the control simulation (dashed) are shown as reference.

Changes in the aerosol number concentrations available for homogeneous freezing (simulations LSUC and HSUC; see Figure 9d) have virtually no impact on the vertical cirrus cloud profile or the cirrus IWP in the model simulations. The explanation for the low sensitivity of the cirrus properties to the aerosol number concentrations is that ice crystals are generated almost entirely through heterogeneous freezing processes with homogeneous freezing playing only a minor role.

However, because heterogeneous ice nucleation dominates in the midlatitude cirrus case, changing the number concentration of aerosols serving as heterogeneous IN significantly impacts the microphysical and macrophysical properties of the cirrus in the simulations with varying IN concentrations (simulations LINC and HINC; see Figure 9e). Lower (higher) IN concentrations lead to lower (higher) ice number concentrations and to lower (higher) values of IWC and IWP by decreasing (increasing) the total surface area of ice crystals available to vapor deposition.

The largest effect on the microphysical properties of the midlatitude cirrus case is observed in the simulations with changing mode of ice nucleation (simulations HOMO and HETO; see Figure 9f). Assuming homogeneous freezing only (HOMO) considerably reduces the thickness of the cloud and, therefore, reduces the IWP. Interestingly, the cirrus cloud profile in the HOMO simulation exhibits the least agreement with observations regarding the thickness of the cloud and the location of peak IWC. In contrast, the

Table 4. Domain-Averaged Values for Ice Water Content (IWC), Ice Number Concentrations (INC), Effective Diameter of Ice Crystals (D_e), Ice Water Path (IWP), Cirrus Cloud Cover (CC), Cirrus Longwave Emissivity (E), Cirrus Transmissivity (T), and Outgoing Longwave Radiation (OLR) for the Midlatitude Cirrus Case[a]

Simulation	IWC (mg m^{-3})	INC (l^{-1})	D_e (μm)	IWP (g m^{-2})	CC (%)	E	T	OLR (W m^{-2})
CTL	14.3	46.9	123.6	88.7	63.4	0.70	0.30	180.1
LIFS	15.9	46.5	124.9	96.4 (8.6)	63.6 (0.3)	0.71 (1.4)	0.29 (−3.3)	179.5 (−0.4)
HIFS	13.2	47.2	122.4	83.7 (−5.6)	63.2 (−0.3)	0.69 (−1.4)	0.31 (3.2)	180.8 (0.4)
LIAC	11.5	44.6	99.5	64.4 (−27.4)	63.4 (0.1)	0.66 (−6.2)	0.34 (14.7)	194.3 (7.9)
HIAC	16.5	46.7	140.6	108.9 (22.7)	63.3 (−0.1)	0.71 (1.3)	0.29 (−3.1)	174.8 (−3.0)
LVDC	14.2	46.7	107.3	92.7 (4.4)	61.9 (−2.4)	0.68 (−3.0)	0.32 (7.1)	192.6 (7.0)
HVDC	14.2	47.0	125.0	87.7 (−1.1)	63.5 (0.2)	0.70 (0.1)	0.30 (−0.2)	179.4 (−0.4)
LSUC	14.3	46.9	123.6	88.7 (0.0)	63.4 (0.0)	0.70 (0.0)	0.30 (0.0)	180.1 (0.0)
HSUC	14.3	46.9	123.6	88.7 (0.0)	63.4 (0.0)	0.70 (0.0)	0.30 (0.0)	180.1 (0.0)
LINC	11.2	9.9	149.8	65.2 (−26.6)	62.0 (−2.2)	0.61 (−13.7)	0.39 (32.4)	197.6 (9.7)
HINC	17.2	130.7	107.7	112.8 (27.1)	64.0 (0.9)	0.75 (6.7)	0.25 (−15.8)	172.5 (−4.2)
HOMO	16.0	133.5	180.5	78.1 (−12.0)	46.9 (−26.1)	0.64 (−8.7)	0.36 (20.7)	194.4 (7.9)
HETO	14.3	46.9	123.6	88.7 (0.0)	63.4 (0.0)	0.70 (0.0)	0.30 (0.0)	180.1 (0.0)

[a]Percentage changes with respect to the control simulation are given in parentheses.

simulation with heterogeneous ice nucleation only (HETO) yields a cloud fraction and IWC profile, which is qualitatively in good agreement with the observations. The considerable mismatch between the simulated and observed cirrus cloud profile in the HOMO simulation corroborates the idea that heterogeneous freezing mechanisms may indeed be the dominant ice initiation process in midlatitude cirrus as suggested recently by *Cziczo et al.* [2013]. However, it is noted that the majority of the midlatitude ice residual samples were collected in anvil cirrus and, thus, may not be representative of other genre of midlatitude cirrus or cirrus forming in cleaner oceanic environments as in our case.

Overall, the most pronounced impacts on the vertical cirrus cloud profile and cirrus IWP are seen in the PPE simulations with changing modes of ice nucleation (simulations HOMO and HETO), altered number concentrations of IN available for heterogeneous ice nucleation (simulations LINC and HINC) and changes in the value of the ice deposition coefficient (simulations LVDC and HVDC). Changes in the ice fall speeds (simulations LIFS and HIFS) and the threshold size for the ice autoconversion (simulations LIAC and HIAC) also have a considerable but less prominent effect on the vertical cirrus profiles. The least effect is seen for changes in the number concentrations of sulfate aerosols available for homogeneous freezing (simulations LSUC and HSUC).

In order to investigate the effect of the microphysical sensitivities on the physical properties and radiative impact of cirrus on larger scales, domain-averaged statistics are shown in Figure 11 and Table 4 for each PPE simulation. These statistics are representative of the mesoscale cirrus cloud system rather than individual patches of cirrus. On the larger cloud system scale, cirrus IWP is most sensitive to changes in the number concentrations of IN for heterogeneous ice nucleation, the mode of ice nucleation, and the threshold size for ice autoconversion. Changes in ice fall speeds have a minor impact on the average IWP on larger scales, whereas changing values for the ice deposition coefficient and sulfate aerosol number concentrations have little or no effect (Figure 11a). Interestingly, while cirrus IWP changes are on the order of almost 30% in the midlatitude cirrus case, changes in the cirrus cloud cover are small and on the order of about 2% except in the simulation with homogeneous freezing only (HOMO) where domain-averaged cloud cover drops by about 26% (Figure 11b). Thus, in all PPE simulations with the exception of the HOMO simulation, changes in the radiative impact of cirrus are primarily driven by changes in the cirrus microphysical properties whereas changes in cirrus cloud cover are marginal.

The changes in cirrus IWP induced by the size of microphysical uncertainties also affect the cirrus radiative properties such as the longwave emissivity (Figure 11c) and transmissivity (Figure 11d). Generally, the changes in the longwave emissivities are weaker compared with changes in IWP. The weaker sensitivity in the cirrus longwave emissivity is explained by the relatively large fraction of the cirrus cloud field with emissivities near unity. In other words, a majority of the mesoscale cirrus cloud field is already saturated in terms of emissivity, which limits the sensitivity of the mesoscale field of cirrus clouds as a whole.

Throughout this study, we use cirrus transmissivity as a proxy for OLR directly affected by cirrus. In contrast, OLR is affected by cirrus and other high and midlevel clouds not identified as cirrus by our classification

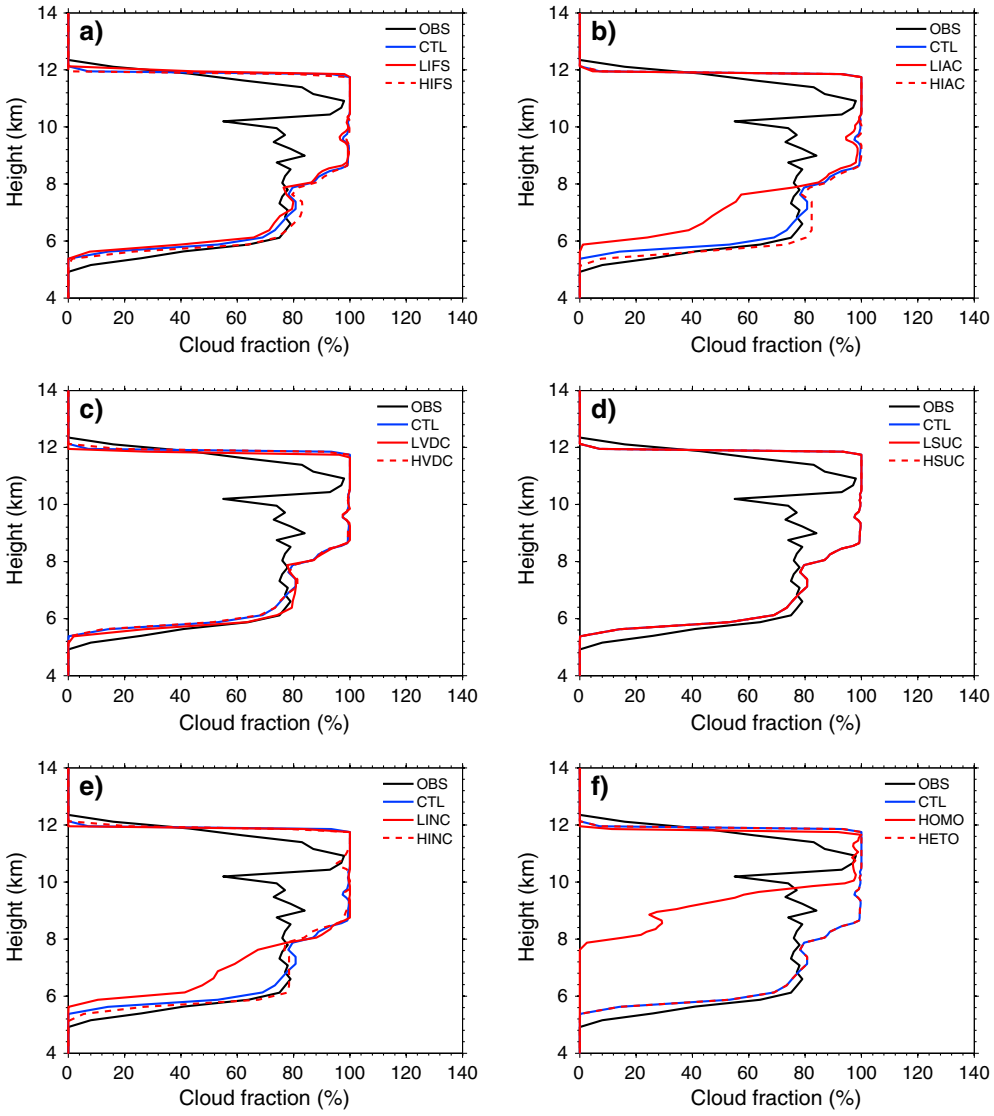

Figure 12. Same as Figure 9 but for the subtropical cirrus case.

scheme. Overall, the changes in IWP translate into consistent changes in terms of cirrus emissivity and transmissivity but the impact on OLR is damped due to the contributions from clouds other than cirrus and does not exceed 10% in the midlatitude cirrus case (Figure 11e). The largest sensitivities regarding the radiative impact of midlatitude cirrus are caused by uncertainties in ice nucleation, in particular, the number concentrations of IN for heterogeneous ice nucleation, and the mode of ice nucleation (i.e., homogeneous freezing versus heterogeneous freezing) whereas the ice autoconversion threshold size and the fall speeds of ice particles only have a moderate to minor effect on the radiative impact of the cirrus cloud field on larger scales. Changes in the values of the ice deposition coefficient affect the radiative impact of cirrus only for very low values on the order of about 0.005 whereas changes in sulfate aerosol concentrations have no effect at all.

6.2. Subtropical Cirrus Case

The sensitivity of the subtropical cirrus cloud fraction and IWC profiles in the PPE simulations is shown in Figures 12 and 13, respectively. Domain-averaged statistics for the subtropical cirrus case are summarized in Table 5. Similar to the midlatitude cirrus case, the largest variability in the cirrus properties are seen for changes in the mode of ice nucleation (simulations HOMO and HETO), changes in the IN concentrations (simulations LINC and HINC), and changes in the threshold size for ice autoconversion (simulation LIAC and HIAC). Changes in the ice fall speeds (simulations LIFS and HIFS) have only a minor impact on the cirrus cloud profile or the cirrus IWP whereas changes in the value of the ice deposition (simulations LVDC and

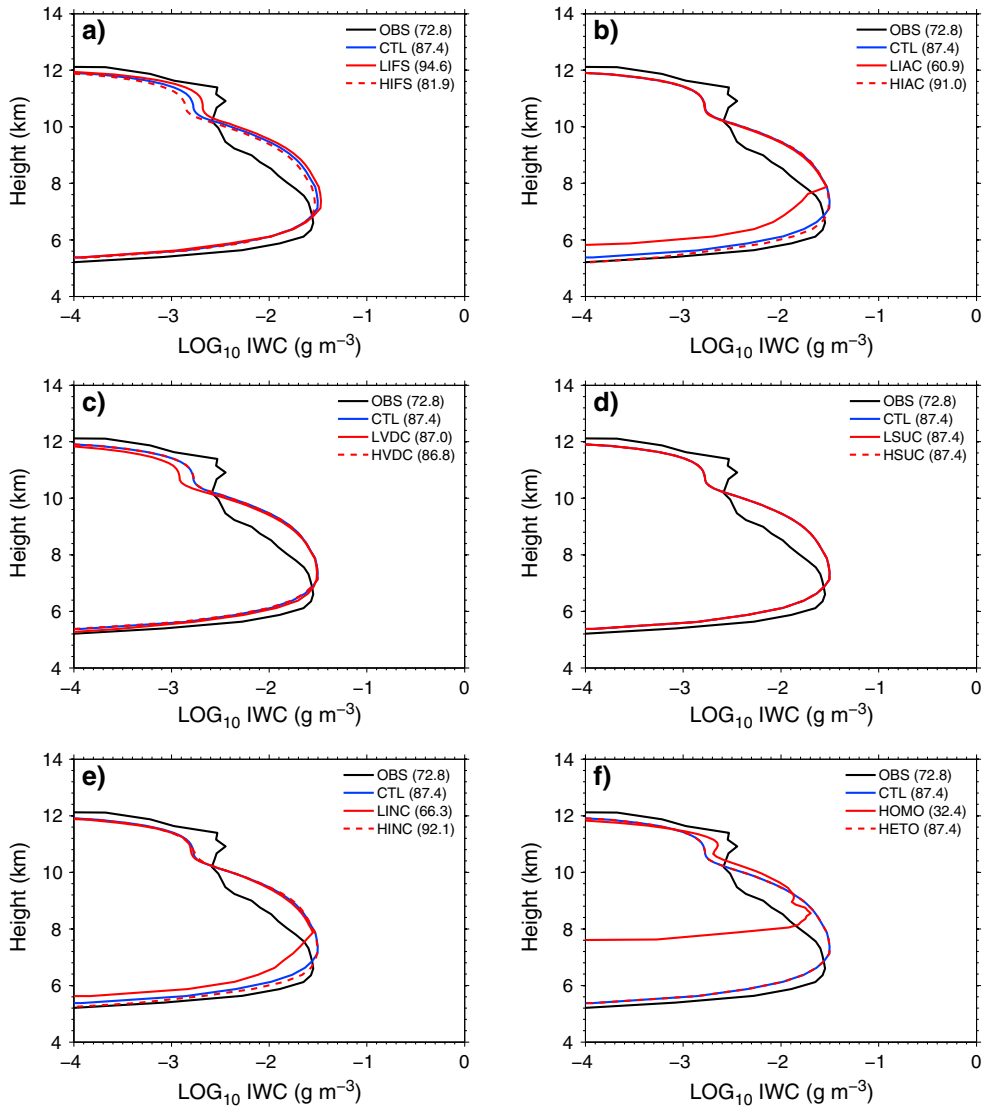

Figure 13. Same as Figure 10 but for the subtropical cirrus case.

Table 5. Domain-Averaged Values for Ice Water Content (IWC), Ice Number Concentrations (INC), Effective Diameter of Ice Crystals (D_e), Ice Water Path (IWP), Cirrus Cloud Cover (CC), Cirrus Longwave Emissivity (E), Cirrus Transmissivity (T), and Outgoing Longwave Radiation (OLR) for the Subtropical Cirrus Case[a]

Simulation	IWC (mg m^{-3})	INC (l^{-1})	D_e (μm)	IWP (g m^{-2})	CC (%)	E	T	OLR (W m^{-2})
CTL	4.7	39.1	89.8	20.2	81.3	0.34	0.66	239.0
LIFS	5.3	38.2	89.3	21.9 (8.3)	82.8 (1.9)	0.36 (3.5)	0.64 (−1.8)	239.1 (0.0)
HIFS	4.2	39.9	90.5	18.8 (−7.1)	79.9 (−1.7)	0.33 (−3.2)	0.67 (1.7)	239.0 (−0.0)
LIAC	4.3	38.5	76.0	17.0 (−15.8)	81.2 (−0.1)	0.32 (−6.4)	0.68 (3.4)	245.0 (2.5)
HIAC	4.8	39.0	97.9	20.9 (3.6)	81.3 (−0.0)	0.35 (2.0)	0.65 (−1.0)	236.8 (−0.9)
LVDC	4.3	40.6	66.0	19.2 (−5.0)	77.2 (−5.0)	0.31 (−8.9)	0.69 (4.7)	250.5 (4.8)
HVDC	4.7	38.8	92.4	20.2 (−0.2)	82.0 (0.9)	0.35 (0.2)	0.65 (−0.1)	238.1 (−0.4)
LSUC	4.7	39.1	89.8	20.2 (0.0)	81.3 (0.0)	0.34 (0.0)	0.66 (0.0)	239.0 (0.0)
HSUC	4.7	39.1	89.8	20.2 (0.0)	81.3 (0.0)	0.34 (0.0)	0.66 (0.0)	239.0 (0.0)
LINC	3.7	8.9	114.1	15.5 (−23.1)	76.7 (−5.7)	0.26 (−24.9)	0.74 (13.1)	248.5 (3.9)
HINC	5.1	108.8	74.8	21.3 (5.6)	84.2 (3.6)	0.40 (14.9)	0.60 (−7.8)	235.4 (−1.5)
HOMO	3.3	44.6	163.3	13.8 (−31.5)	18.0 (−77.9)	0.30 (−12.6)	0.70 (6.6)	250.4 (4.8)
HETO	4.7	39.1	89.8	20.2 (0.0)	81.3 (0.0)	0.34 (0.0)	0.66 (0.0)	239.0 (0.0)

[a]Percentage changes with respect to the control simulation are given in parentheses.

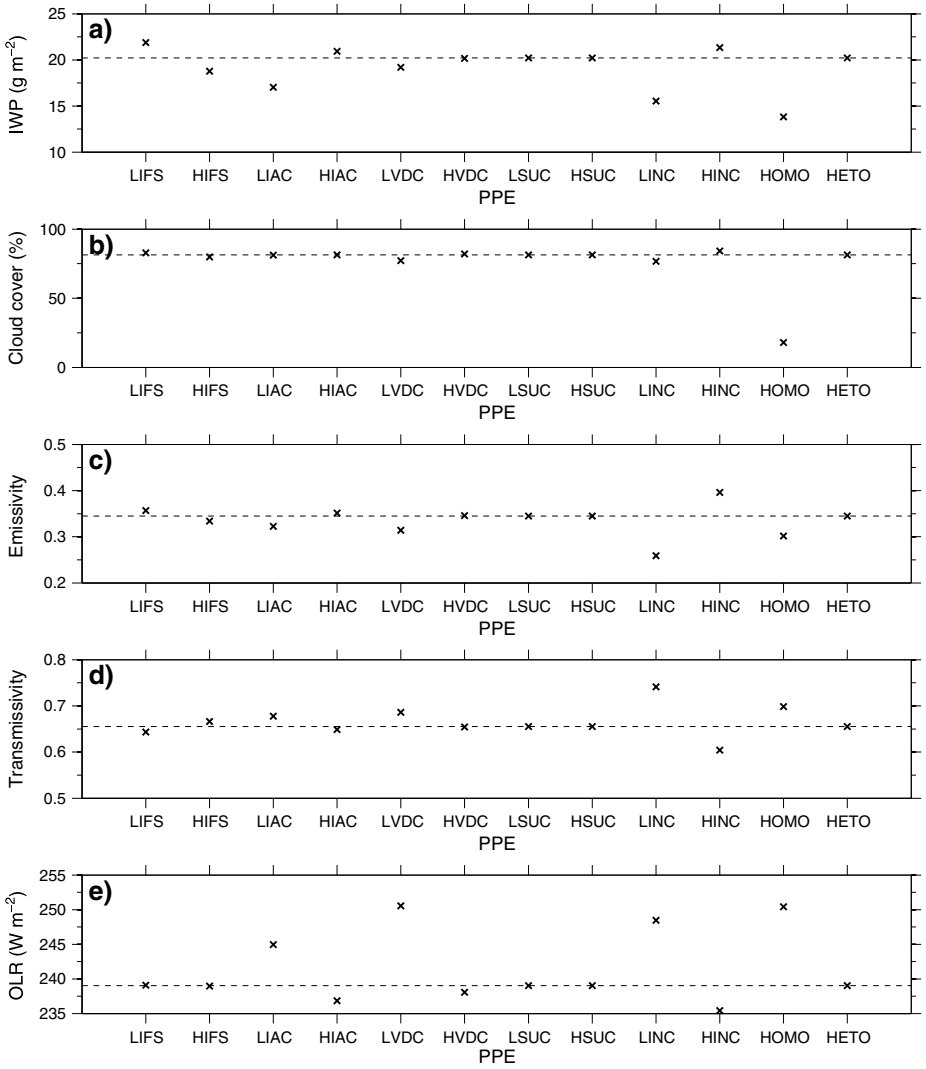

Figure 14. Same as Figure 11 but for the subtropical cirrus case.

HVDC) and the number concentrations of sulfate aerosols (simulations LSUC and HSUC) have no impact on the cirrus cloud profile or the IWP.

In the simulation with homogeneous freezing only (HOMO), the thickness of the subtropical cirrus cloud layer is reduced to about 2 km and the IWP is much lower than observations suggest. In contrast, the cirrus cloud profile in the simulation with heterogeneous ice nucleation only (HETO) is thicker and agrees better with the observations. Similar to the midlatitude cirrus case, heterogeneous ice nucleation is the dominant freezing mechanisms in the simulations with homogeneous freezing playing only a minor role. As a consequence, the subtropical cirrus cloud layer exhibits virtually no sensitivity to changes in the sulfate aerosol concentrations available to homogeneous freezing but considerable sensitivity to the number concentration of IN available for heterogeneous freezing. On larger scales, the microphysical uncertainties causing the largest change of the radiative impact of the subtropical cirrus cloud system is the mode of ice nucleation (Figure 14). Assuming homogeneous freezing not only reduces the thickness of the cirrus layers and the cirrus IWP but also leads to a considerably reduced cirrus cloud cover. For all other microphysical changes, cirrus cloud cover is only marginally affected and changes in the cirrus radiative impact are caused almost entirely by changes in the microphysical properties such as the IWP and the effective radius of ice particles.

6.3. Tropical Cirrus Case

Figures 15 and 16 show the variability of the cirrus cloud fraction and IWC profiles in the PPE simulations for the tropical cirrus case. Domain-averaged statistics for the tropical cirrus case are summarized in Table 6.

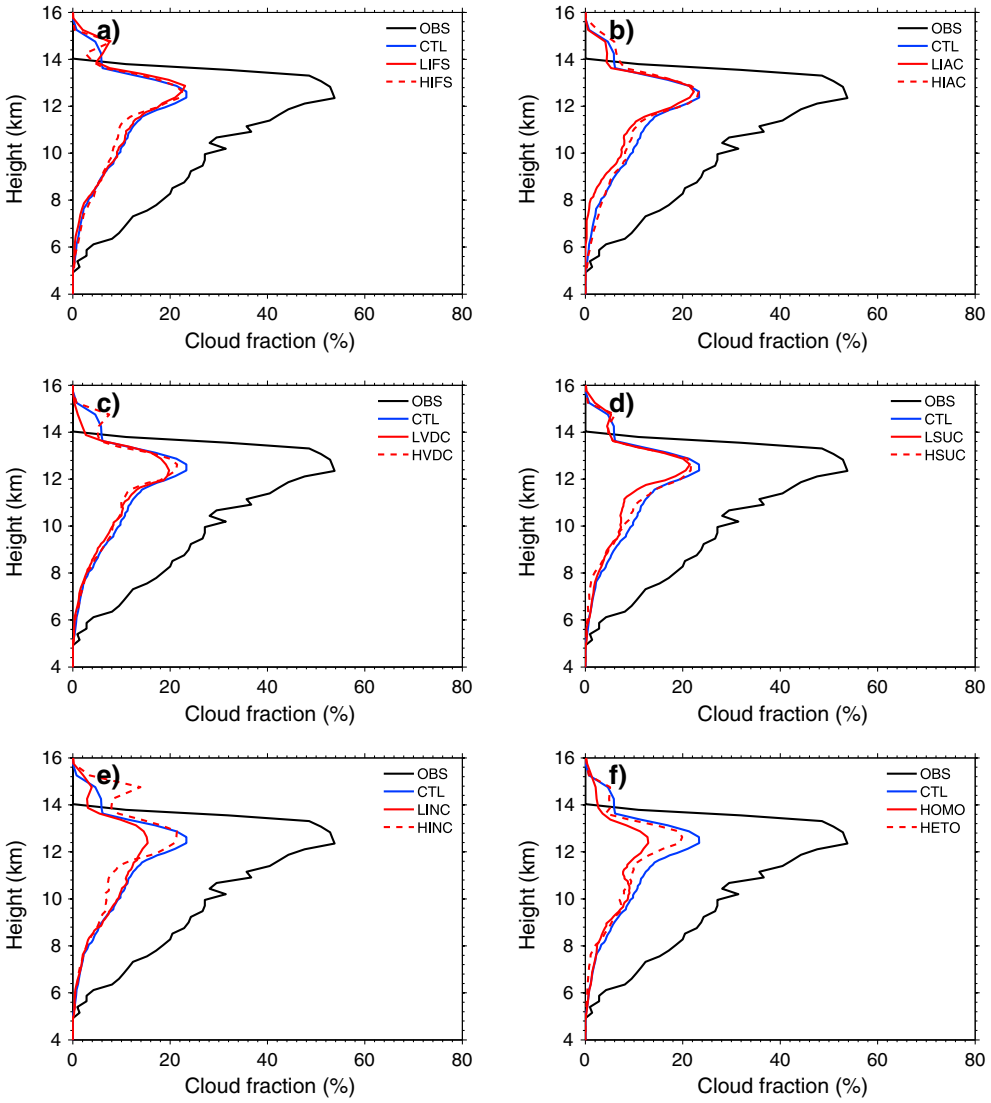

Figure 15. Same as Figure 9 but for the tropical cirrus case.

Similar to the midlatitude and subtropical cirrus cases, the largest sensitivities in terms of the vertical cirrus cloud profile and cirrus IWP are observed in the simulations with changing ice autoconversion threshold size (LIAC and HIAC), changing ice nucleation modes (HOMO and HETO), and changing IN number concentrations (LINC and HINC). Changes in the value of the ice deposition coefficient (LVDC and HVDC) have a significant but small effect on the cirrus cloud profile in the study region and, similar to the midlatitude cirrus case, the effect is transient and fades over time with little impact on the cirrus IWP or the radiative effect of cirrus on larger scales. Interestingly, the tropical anvil cirrus case is the only case where altering the number concentrations of sulfate aerosols (LSUC and HSUC) has a significant and persistent effect on the physical and radiative properties of cirrus.

Similar to the midlatitude and subtropical cirrus cases, perturbing the microphysics in the anvil cirrus case affects the distribution of IWC in the entire cirrus cloud layer. However, contrary to the other cases, the height of cloud base is rather insensitive to microphysical perturbations in the anvil cirrus case except in the simulations with changing ice autoconversion threshold size (LIAC and HIAC). Overall, there is relatively little impact on the emissivity and transmissivity of the anvil cirrus and cloud cover is only marginally affected (Figure 17). The only exception is the simulation with homogeneous freezing only (HOMO), which exhibits substantially higher IWP and lower cirrus cloud cover. The higher IWP and lower cloud cover are explained by the fact that the high ice supersaturations necessary to initiate ice crystals homogeneously

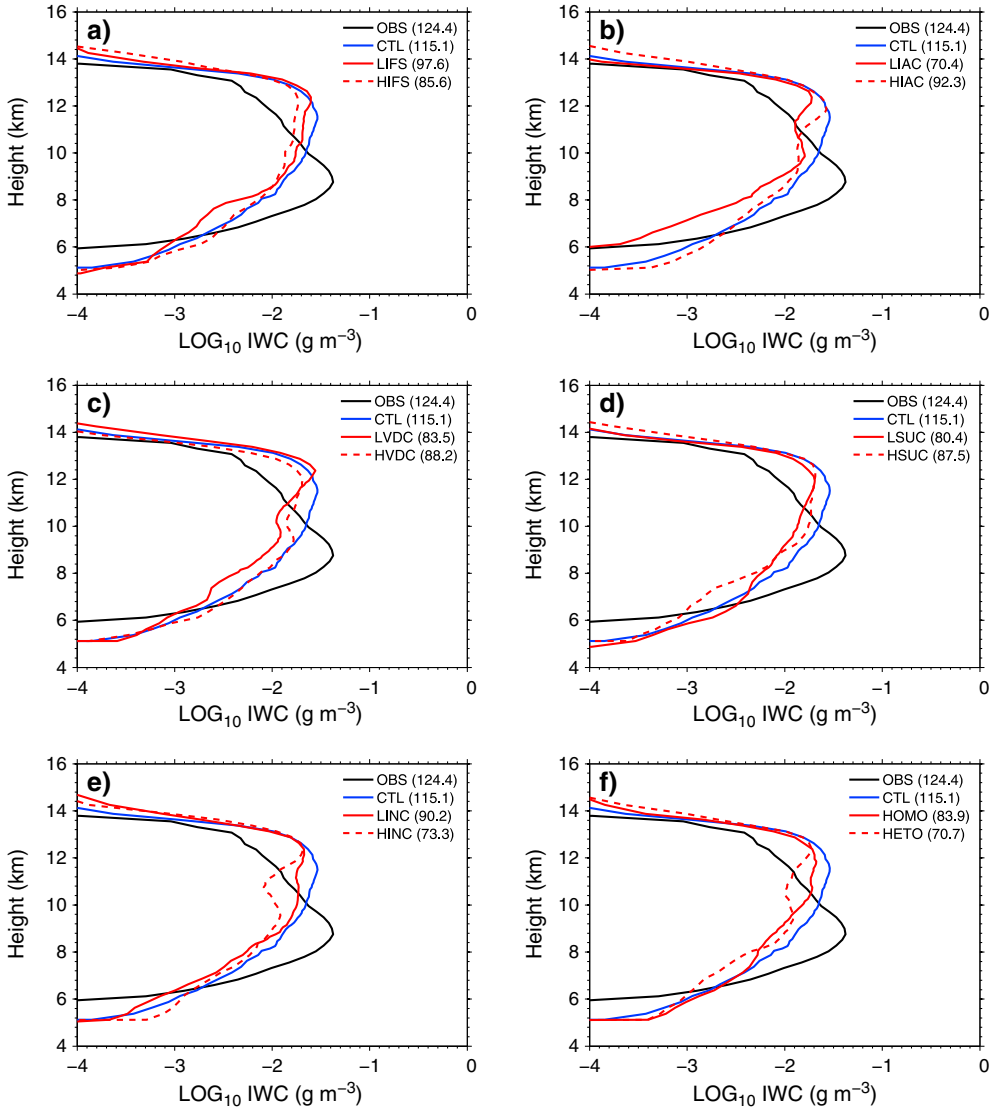

Figure 16. Same as Figure 10 but for the tropical cirrus case.

Table 6. Domain-Averaged Values for Ice Water Content (IWC), Ice Number Concentrations (INC), Effective Diameter of Ice Crystals (D_e), Ice Water Path (IWP), Cirrus Cloud Cover (CC), Cirrus Longwave Emissivity (E), Cirrus transmissivity (T), and Outgoing Longwave Radiation (OLR) for the Tropical Cirrus Case[a]

Simulation	IWC (mg m^{-3})	INC (l^{-1})	D_e (μm)	IWP (g m^{-2})	CC (%)	E	T	OLR (W m^{-2})
CTL	69.4	76.5	97.9	130.9	18.2	0.30	0.70	239.8
LIFS	73.0	83.3	97.4	131.8 (0.7)	19.1 (4.8)	0.30 (−0.3)	0.70 (0.1)	242.0 (0.9)
HIFS	64.6	70.5	97.5	130.1 (−0.6)	17.3 (−5.0)	0.30 (0.6)	0.70 (−0.2)	239.4 (−0.2)
LIAC	65.1	69.0	80.7	118.7 (−9.3)	18.7 (2.5)	0.31 (1.7)	0.69 (−0.7)	244.0 (1.7)
HIAC	70.0	85.1	108.6	137.8 (5.3)	17.8 (−2.2)	0.31 (1.4)	0.69 (−0.6)	237.7 (−0.9)
LVDC	67.3	103.8	91.8	138.4 (5.7)	16.8 (−7.4)	0.32 (4.1)	0.68 (−1.8)	238.7 (−0.5)
HVDC	71.5	80.8	98.1	134.7 (2.9)	18.3 (0.7)	0.30 (−1.8)	0.70 (0.8)	240.3 (0.2)
LSUC	71.1	78.0	97.9	136.5 (4.3)	18.2 (−0.2)	0.30 (−0.9)	0.70 (0.4)	239.6 (−0.1)
HSUC	68.4	75.0	96.5	132.1 (0.9)	17.8 (−2.0)	0.30 (−0.3)	0.70 (0.1)	239.8 (−0.0)
LINC	69.4	57.1	113.3	152.0 (16.2)	15.1 (−16.9)	0.32 (5.7)	0.68 (−2.5)	240.2 (0.1)
HINC	70.9	135.8	84.1	126.0 (−3.7)	19.8 (8.5)	0.31 (2.2)	0.69 (−1.0)	241.3 (0.6)
HOMO	109.9	75.7	197.4	299.5 (128.9)	6.9 (−62.2)	0.50 (65.2)	0.50 (−28.3)	223.3 (−6.9)
HETO	69.4	73.8	96.7	131.5 (0.5)	18.0 (−1.0)	0.30 (−1.0)	0.70 (0.4)	239.6 (−0.1)

[a]Percentage changes with respect to the control simulation are given in parentheses.

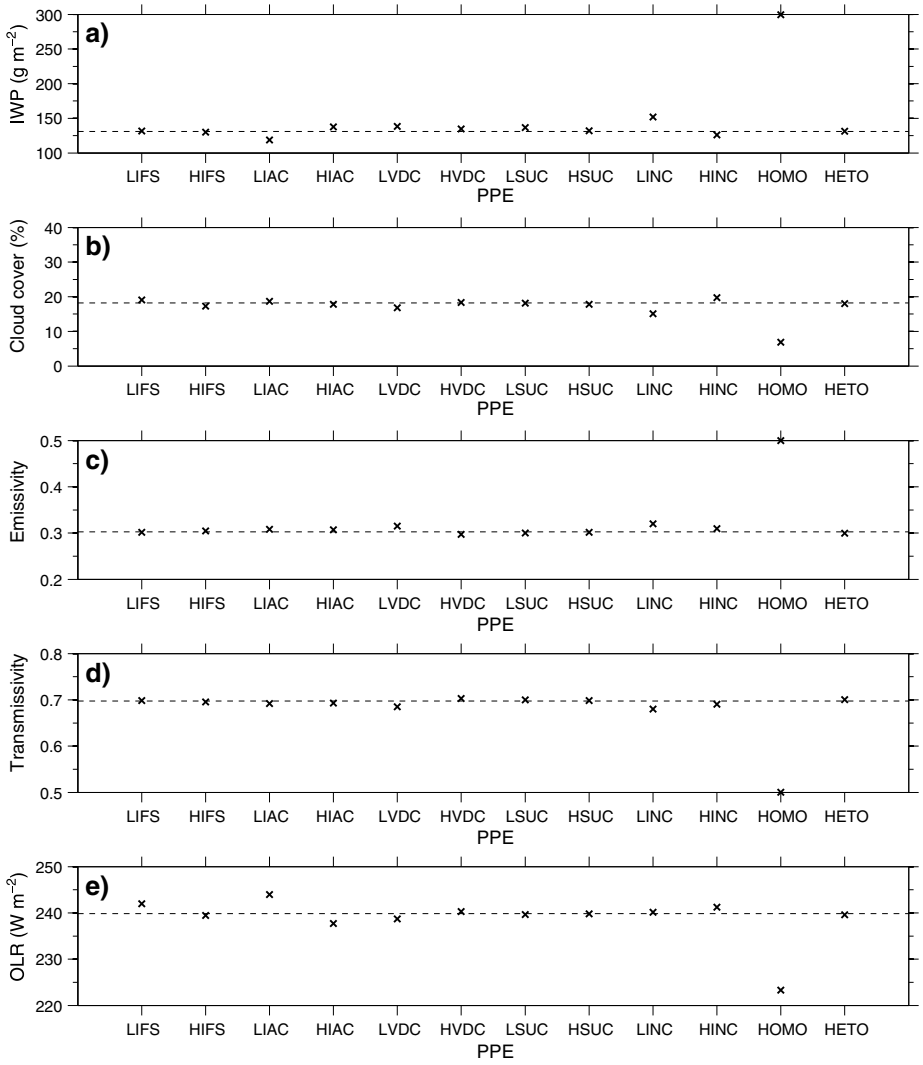

Figure 17. Same as Figure 11 but for the tropical cirrus case.

lead to higher depositional growth rates, which, in turn, increase the IWC and average size of ice particles thereby increasing also ice fall speeds. The larger ice sedimentation losses lead to anvil clouds more localized around the cores of the tropical convective towers by limiting the horizontal divergence of the anvil cirrus.

Overall, changing the parameters in the ice microphysics has some effect on the cirrus IWP but little impact on the cirrus cloud cover, the cirrus transmissivity, and the OLR of the mesoscale field of clouds (Figure 17). In fact, relative changes in cirrus IWP are typically less than 10%, whereas changes in the cloud cover and transmissivity of cirrus are less than 3% and do not exceed 2% for OLR in all PPEs except the simulation with homogeneous freezing only (HOMO).

7. Conclusions

In this study, the effect of uncertainties in parameterized ice microphysics and initial conditions on the microphysical properties and radiative impact of cirrus is investigated by means of PPE and ICE simulations on the cloud system-resolving scale. Three cirrus cases representing typical environmental conditions at midlatitudes, subtropics, and tropics are examined.

We find that for midlatitude and subtropical cirrus, the variability induced by perturbing uncertain parameters in ice microphysics parameterizations clearly outweighs the variability induced by perturbing initial

conditions. However, for tropical anvil cirrus, the microphysical sensitivity with respect to varying initial conditions is considerably larger and about the same order of magnitude as in the PPE simulations. This result emphasizes the sensitivity of anvil cirrus microphysics to the dynamics of deep convective systems in the tropics.

Overall, substantial sensitivities in the microphysical and macrophysical properties of cirrus to uncertainties in the parameterized ice microphysics are found for the vertical distribution of cloud fraction and IWC as well as cloud thickness and IWP whereas in most cases cirrus cloud cover is only marginally affected. Changes in cirrus IWP are primarily controlled by changes in the vertical distribution of IWC and to a lesser degree by changes in cloud thickness. The result that cirrus cloud cover is only marginally affected suggests that GCMs may overestimate the sensitivity of high cloud cover to uncertainties in ice microphysics and its impact on the radiative forcing of cirrus on a global scale.

In all cirrus cases, the top three physical uncertainties controlling the variability of the microphysical and radiative properties of cirrus as well as the radiative impact of cirrus cloud fields on larger scales are the mode of ice nucleation (homogeneous versus heterogeneous ice nucleation), the number concentrations of IN available for heterogeneous ice nucleation, and the threshold size of ice particles used in the parameterization of ice autoconversion. Uncertainties in ice fall speeds are found to be of minor importance relative to other microphysical uncertainties such as ice nucleation. This results stems from the fact that Doppler radar observations have led to better constrained retrievals of ice fall speeds and substantially improved ice fall speed parameterizations in recent years. We note, however, that even for the very small changes in ice crystal fall speed that we made, we found a variability in IWP of up to 15%. This is illustrative of the extreme sensitivity to this parameter found in other PPE experiments performed with GCMs such as *Sanderson et al.* [2008].

Uncertainties in the value of the ice deposition coefficient are found to play a minor role for the radiative impact of mesoscale cirrus cloud fields because most of the effects are transient and do not persist over longer time scales except in cases of very low ice deposition coefficients on the order of about 0.005. The impact of changes in sulfate aerosol number concentrations available for homogeneous freezing is negligible for midlatitude and subtropical cirrus and is substantial for tropical anvil cirrus only. Tropical anvil cirrus are found as the only cirrus category sensitive to changes in the sulfate aerosol number concentrations because homogeneous freezing plays a minor role for ice initiation in the simulations of the midlatitude and subtropical cirrus case. We also find that assuming homogeneous freezing as the sole ice nucleation mechanisms yields cirrus cloud profiles in strong disagreement with observations in the midlatitude and subtropical cirrus case. However, assuming heterogeneous ice nucleation only explains the observed cirrus cloud profiles to a reasonable degree.

The results of the PPE simulations suggest that recently improved parameterizations of ice fall speeds greatly constrain uncertainties regarding the microphysical properties and radiative impact of cirrus clouds. In the future, observational resources should be focused on constraining uncertainties in ice nucleation processes, providing improved measurements of ice particle size distributions as well as size distributions and chemical composition of aerosols in the upper troposphere. These types of measurements are necessary for improving ice microphysics parameterizations in numerical models across scales.

Acknowledgments

The authors gratefully acknowledge the constructive comments and suggestions made by five anonymous reviewers, which greatly helped to improve the manuscript. The first author thanks Hugh Morrison (NCAR) for providing the double-moment cloud microphysics code. This work is facilitated through the use of advanced computational, storage, and networking infrastructures provided by the Hyak supercomputer system, supported in part by the University of Washington eScience Institute. We also acknowledge high-performance computing support provided by NCAR's Computational and Information Systems Laboratory (CISL), sponsored by the National Science Foundation (NSF). This research is supported through funding from NASA grant NNX10AM79G and NSF grant 1144017. The publication is partially funded by the Joint Institute for the Study of the Atmosphere and Ocean (JISAO) under cooperative agreement NA10OAR4320148, contribution 2154.

References

Ackerman, T. P., K. N. Liou, F. P. J. Valero, and L. Pfister (1988), Heating rates in tropical anvils, *J. Atmos. Sci.*, *45*(10), 1606–1623.

Baldauf, M., A. Seifert, J. Foerstner, D. Majewski, M. Raschendorfer, and T. Reinhardt (2011), Operational convective-scale numerical weather prediction with the COSMO model: Description and sensitivities, *Mon. Weather Rev.*, *139*(12), 3887–3905.

Berry, E., and G. G. Mace (2013), Cirrus cloud properties and the large-scale meteorological environment: Relationships derived from A-Train and NCEP-NCAR Reanalysis data, *J. Appl. Meteorol. Clim.*, *52*(5), 1253–1276.

Bodas-Salcedo, A., et al. (2011), Cosp Satellite simulation software for model assessment, *Bull. Am. Meteorol. Soc.*, *92*(8), 1023–1043.

Bott, A. (1989), A positive definite advection scheme obtained by nonlinear renormalization of the advective fluxes, *Mon. Weather Rev.*, *117*(6), 1006–1015.

Cziczo, D. J., K. D. Froyd, C. Hoose, E. J. Jensen, M. Diao, M. A. Zondlo, J. B. Smith, C. H. Twohy, and D. M. Murphy (2013), Clarifying the dominant sources and mechanisms of cirrus cloud formation, *Science*, *340*(6138), 1320–1324.

DeMott, P. J., A. J. Prenni, X. Liu, S. M. Kreidenweis, M. D. Petters, C. H. Twohy, M. S. Richardson, T. Eidhammer, and D. C. Rogers (2010), Predicting global atmospheric ice nuclei distributions and their impacts on climate, *Proc. Natl. Acad. Sci. U.S.A.*, *107*(25), 11,217–11,222.

Deng, M., and G. G. Mace (2008), Cirrus cloud microphysical properties and air motion statistics using cloud radar Doppler moments: Water content, particle size, and sedimentation relationships, *Geophys. Res. Lett.*, *35*, L17808, doi:10.1029/2008GL035054.

Doms, G., and U. Schättler (2002), A description of the nonhydrostatic regional model LM. Part I: Dynamics and numerics, *Tech. Rep.*, Deutscher Wetterdienst, Offenbach, Germany.

Gettelman, A., X. Liu, S. J. Ghan, H. Morrison, S. Park, A. J. Conley, S. A. Klein, J. Boyle, D. L. Mitchell, and J. L. F. Li (2010), Global simulations of ice nucleation and ice supersaturation with an improved cloud scheme in the Community Atmosphere Model, *J. Geophys. Res.*, *115*, D18216, doi:10.1029/2009JD013797.

Gettelman, A., X. Liu, D. Barahona, U. Lohmann, and C. Chen (2012), Climate impacts of ice nucleation, *J. Geophys. Res.*, *117*, D20201, doi:10.1029/2012JD017950.

Gierens, K. M., M. Monier, and J. F. Gayet (2003), The deposition coefficient and its role for cirrus clouds, *J. Geophys. Res.*, *108*(D2), 4069, doi:10.1029/2001JD001558.

Haag, W., B. Kärcher, J. Ström, A. Minikin, U. Lohmann, J. Ovarlez, and A. Stohl (2003), *Atmos. Chem. Phys.*, *3*, 1791–1806.

Harrington, J. Y., D. Lamb, and R. Carver (2009), Parameterization of surface kinetic effects for bulk microphysical models: Influences on simulated cirrus dynamics and structure, *J. Geophys. Res.*, *114*, D06212, doi:10.1029/2008JD011050.

Heymsfield, A. J. (2003), Properties of tropical and midlatitude ice cloud particle ensembles. Part I: Median mass diameters and terminal velocities, *J. Atmos. Sci.*, *60*(21), 2573–2591.

Heymsfield, A. J., A. Bansemer, P. R. Field, S. L. Durden, J. L. Stith, J. E. Dye, W. Hall, and C. A. Grainger (2002), Observations and parameterizations of particle size distributions in deep tropical cirrus and stratiform precipitating clouds: Results from in situ observations in TRMM field campaigns, *J. Atmos. Sci.*, *59*(24), 3457–3491.

Hoose, C., and O. Mohler (2012), Heterogeneous ice nucleation on atmospheric aerosols: A review of results from laboratory experiments, *Atmos. Chem. Phys.*, *12*, 9817–9854.

Im, E., S. L. Durden, and C. Wu (2006), Cloud profiling radar for the CloudSat mission, *IEEE Aerosp. Electron. Syst. Mag.*, *20*, 15–18.

Jensen, E., et al. (1998), Ice nucleation processes in upper tropospheric wave-clouds observed during SUCCESS, *Geophys. Res. Lett.*, *25*, 1363–1366.

Jensen, E. J., L. Pfister, T.-P. Bui, P. Lawson, and D. Baumgardner (2010), Ice nucleation and cloud microphysical properties in tropical tropopause layer cirrus, *Atmos. Chem. Phys.*, *10*(3), 1369–1384.

Joos, H., P. Spichtinger, U. Lohmann, J. F. Gayet, and A. Minikin (2008), Orographic cirrus in the global climate model ECHAM5, *J. Geophys. Res.*, *113*, D18205, doi:10.1029/2007JD009605.

Karcher, B., and J. Strom (2003), The roles of dynamical variability and aerosols in cirrus cloud formation, *Atmos. Chem. Phys.*, *3*, 823–838.

Kay, J. E., and R. Wood (2008), Timescale analysis of aerosol sensitivity during homogeneous freezing and implications for upper tropospheric water vapor budgets, *Geophys. Res. Lett.*, *35*, L10809, doi:10.1029/2007GL032628.

Khvorostyanov, V. I., and J. A. Curry (2002), Terminal velocities of droplets and crystals: Power laws with continuous parameters over the size spectrum, *J. Atmos. Sci.*, *59*, 1872–1884.

Koop, T., B. P. Luo, A. Tsias, and T. Peter (2000), Water activity as the determinant for homogeneous ice nucleation in aqueous solutions, *Nature*, *406*(6796), 611–614.

Kulkarni, G., J. Fan, J. M. Comstock, X. Liu, and M. Ovchinnikov (2012), Laboratory measurements and model sensitivity studies of dust deposition ice nucleation, *Atmos. Chem. Phys.*, *12*(16), 7295–7308.

Liu, X., X. Shi, K. Zhang, E. J. Jensen, A. Gettelman, D. Barahona, A. Nenes, and P. Lawson (2012), Sensitivity studies of dust ice nuclei effect on cirrus clouds with the Community Atmosphere Model CAM5, *Atmos. Chem. Phys.*, *12*, 12,061–12,079.

Lohmann, U., P. Spichtinger, S. Jess, T. Peter, and H. Smit (2008), Cirrus cloud formation and ice supersaturated regions in a global climate model, *Environ. Res. Lett.*, *3*(4), 045,022.

Mace, G. G. (2010), Cloud properties and radiative forcing over the maritime storm tracks of the Southern Ocean and North Atlantic derived from A-Train, *J. Geophys. Res.*, *115*, D10201, doi:10.1029/2009JD012517.

Mace, G. G., S. Benson, and E. Vernon (2006), Cirrus clouds and the large-scale atmospheric state: Relationships revealed by six years of ground-based data, *J. Clim.*, *19*(13), 3257–3278.

Mace, G. G., Q. Zhang, M. Vaughan, R. Marchand, G. Stephens, C. Trepte, and D. Winker (2009), A description of hydrometeor layer occurrence statistics derived from the first year of merged Cloudsat and CALIPSO data, *J. Geophys. Res.*, *114*, D00A26, doi:10.1029/2007JD009755.

Magee, N., A. M. Moyle, and D. Lamb (2006), Experimental determination of the deposition coefficient of small cirrus-like ice crystals near-50° C, *J. Geophys. Res.*, *33*, L17813, doi:10.1029/2006GL026665.

Miloshevich, L. M., H. Vömel, A. Paukkunen, A. J. Heymsfield, and S. J. Oltmans (2003), Characterization and correction of relative humidity measurements from Vaisala RS80-A radiosondes at cold temperatures, *J. Atmos. Oceanic Technol.*, *18*, 135–156.

Minikin, A., A. Petzold, J. Strom, R. Krejci, M. Seifert, P. van Velthoven, H. Schlager, and U. Schumann (2003), Aircraft observations of the upper tropospheric fine particle aerosol in the Northern and Southern Hemispheres at midlatitudes, *Geophys. Res. Lett.*, *30*(10), 1503, doi:10.1029/2002GL016458.

Mitchell, D. L., P. Rasch, D. Ivanova, G. McFarquhar, and T. Nousiainen (2008), Impact of small ice crystal assumptions on ice sedimentation rates in cirrus clouds and GCM simulations, *Geophys. Res. Lett.*, *35*, L09806, doi:10.1029/2008GL033552.

Mitchell, D. L., S. Mishra, and R. P. Lawson (2011), Representing the ice fall speed in climate models: Results from Tropical Composition, Cloud and Climate Coupling (TC4) and the Indirect and Semi-Direct Aerosol Campaign (ISDAC), *J. Geophys. Res.*, *116*, D00T03, doi:10.1029/2010JD015433.

Morrison, H., and A. Gettelman (2008), A new two-moment bulk stratiform cloud microphysics scheme in the Community Atmosphere Model, version 3 (CAM3). Part I: Description and numerical tests, *J. Clim.*, *21*(15), 3642–3659.

Morrison, H., J. A. Curry, and V. I. Khvorostyanov (2005), A new double-moment microphysics parameterization for application in cloud and climate models. Part I: Description, *J. Atmos. Sci.*, *62*(6), 1665–1677.

Morrison, H., G. Thompson, and V. Tatarskii (2009), Impact of cloud microphysics on the development of trailing stratiform precipitation in a simulated squall line: Comparison of one- and two-moment schemes, *Mon. Weather Rev.*, *137*(3), 991–1007.

Muhlbauer, A., T. P. Ackerman, J. M. Comstock, G. S. Diskin, S. M. Evans, R. P. Lawson, and R. T. Marchand (2014), Impact of large-scale dynamics on the microphysical properties of midlatitude cirrus, *J. Geophys. Res. Atmos.*, *119*, doi:10.1002/2013JD020035.

Murphy, D. M., and T. Koop (2005), Review of the vapour pressure of ice and supercooled water for atmospheric applications, *Q. J. R. Meteorol. Soc.*, *131*, 1539–1565.

Murphy, D. M., D. M. Thomson, and M. J. Mahoney (1998), In situ measurements of organics, meteoritic material, mercury, and other elements in aerosols at 5 to 19 kilometers, *Science*, *282*, 1664–1669, doi:10.1126/science.282.5394.1664.

Murphy, J. M., D. M. H. Sexton, D. N. Barnett, G. S. Jones, M. J. Webb, and D. A. Stainforth (2004), Quantification of modelling uncertainties in a large ensemble of climate change simulations, *Nature*, *430*(7001), 768–772.

Reisner, J., R. Rasmussen, and R. Bruintjes (1998), Explicit forecasting of supercooled liquid water in winter storms using the MM5 mesoscale model, *Q. J. R. Meteorol. Soc.*, *124*, 1071–1107.

Ritter, B., and F. Geleyn (1992), A comprehensive radiation scheme for numerical weather prediction models with potential applications in climate simulations, *Mon. Weather Rev.*, *120*, 303–325.

Sanderson, B. M., C. Piani, W. Ingram, D. A. Stone, and M. R. Allen (2008), Towards constraining climate sensitivity by linear analysis of feedback patterns in thousands of perturbed-physics GCM simulations, *Clim. Dyn.*, *30*(2–3), 175–190.

Sassen, K., and G. C. Dodd (1988), Homogeneous nucleation rate for highly supercooled cirrus cloud droplets, *J. Atmos. Sci.*, *45*(8), 1357–1369.

Sassen, K., Z. Wang, and D. Liu (2008), Global distribution of cirrus clouds from CloudSat/Cloud-Aerosol Lidar and Infrared Pathfinder Satellite Observations (CALIPSO) measurements, *J. Geophys. Res.*, *113*, D00A12, doi:10.1029/2008JD009972.

Schmetz, J., P. Pili, S. Tjemkes, D. Just, J. Kerkmann, S. Rota, and A. Ratier (2002), An introduction to Meteosat Second Generation (MSG), *Bull. Am. Meteorol. Soc.*, *83*(7), 977–992.

Stephens, G. L., S. C. Tsay, P. W. Stackhouse, and P. J. Flatau (1990), The relevance of the microphysical and radiative properties of cirrus clouds to climate and climatic feedback, *J. Atmos. Sci.*, *47*(14), 1742–1753.

Tanelli, S., S. L. Durden, E. Im, K. S. Pak, D. G. Reinke, P. Partain, J. M. Haynes, and R. T. Marchand (2008), CloudSats cloud profiling radar after two years in orbit: Performance, calibration, and processing, *IEEE Trans. Geosci. Remote Sens.*, *46*(11), 3560–3573.

Tiedtke, M. (1989), A comprehensive mass flux scheme for cumulus parameterization in large-scale models, *Mon. Weather Rev.*, *117*, 1779–1800.

Turner, D. D., B. M. Lesht, S. A. Clough, J. C. Liljegren, H. E. Revercomb, and D. C. Tobin (2003), Dry bias and variability in Vaisala RS80-H radiosondes: The ARM experience, *J. Atmos. Oceanic Technol.*, *20*, 117–132.

Wicker, L. J., and W. C. Skamarock (2002), Time-splitting methods for elastic models using forward time schemes, *Mon. Weather Rev.*, *130*(8), 2088–2097.

Winker, D. M., W. H. Hunt, and M. J. McGill (2007), Initial performance assessment of CALIOP, *Geophys. Res. Lett.*, *34*(19), L19803, doi:10.1029/2007GL030135.

Wylie, D. P., and W. P. Menzel (1999), Eight years of high cloud statistics using HIRS, *J. Clim.*, *12*(1), 170–184.

Zelinka, M. D., S. A. Klein, and D. L. Hartmann (2012), Computing and partitioning cloud feedbacks using cloud property histograms. Part I: Cloud radiative kernels, *J. Clim.*, *25*(11), 3715–3735.

Zhang, Y., and G. G. Mace (2006), Retrieval of cirrus microphysical properties with a suite of algorithms for airborne and spaceborne lidar, radar, and radiometer data, *J. Appl. Meteorol. Clim.*, *45*(12), 1665–1689.

Zubler, E. M., D. Folini, U. Lohmann, D. Luethi, A. Muhlbauer, S. Pousse-Nottelmann, C. Schaer, and M. Wild (2011), Implementation and evaluation of aerosol and cloud microphysics in a regional climate model, *J. Geophys. Res.*, *116*, D02211, doi:10.1029/2010JD014572.